

Proximal-exploration multi-objective Bayesian optimization for inverse identification of cyclic constitutive law of structural steels

Bach Do · Makoto Ohsaki

Received: date / Accepted: date

Abstract Despite its importance in seismic response analysis, solving an inverse problem to identify the cyclic elastoplastic parameters for structural steels using conventional optimization algorithms still demands a substantial computational cost of repeatedly carrying out many nonlinear analyses. The parameters are commonly identified based on experimental measures from a single loading history, leading them to be biased and giving inaccurate predictions of structural behavior under other loading histories. To address these issues, we formulate a multi-objective inverse problem that simultaneously minimizes the error functions representing the differences between simulated responses and those measured experimentally from various cyclic tests of a steel specimen or a structural component. We then propose proximal-exploration multi-objective Bayesian optimization (MOBO) for solving the formulated inverse problem, resulting in an approximate Pareto front of parameters while limiting the number of costly simulations. MOBO sorts an initial Pareto front and constructs Gaussian process (GP) models for the error functions from a training dataset. It then relies on the hypervolume of the current solutions, the GP models, and a proximal exploration surrounding the current best compromise parameters to formulate an acquisition function that guides the improvement of the current so-

lutions intelligently. Two identification examples show that the parameters obtained from the multi-objective inverse problem can reduce the bias induced by using a single loading history for identification. The robustness of MOBO as well as a good prediction performance of the best compromise solution of identified parameters are demonstrated.

Keywords Elastoplastic constitutive law · Parameter identification · Best compromise parameters · Structural steels · Multi-objective Bayesian optimization · Cyclic loading

1 Introduction

Accurately modeling the cyclic constitutive law for structural steels is a basis for using detailed finite element (FE) models (Ohsaki et al., 2009; Wang et al., 2013) to provide reliable analyses of cyclic elastoplastic behavior of steel structures under earthquake excitation. By parameterizing the constitutive law and incorporating certain material parameters into an appropriate hardening model, for example, isotropic, kinematic, or combined isotropic/kinematic hardening model (Chaboche, 2008; Yoshida et al., 2002), the material parameters are identified based on the available experimental measures of material (or structural) responses before being used as input to other analyses. The problem formulated for finding such parameters is called an inverse problem. Solving this class of problem is computationally expensive from the requirement of repeatedly carrying out many nonlinear response history analyses or static cyclic elastoplastic simulations. Therefore, reducing the computational cost due to repeatedly calling these simulations is of paramount importance in identification of elastoplastic parameters.

Bach Do

Department of Architecture and Architectural Engineering,
Graduate School of Engineering, Kyoto University, Kyoto-
Daigaku Katsura, Nishikyo, Kyoto 615-8540, Japan
E-mail: se.do@archi.kyoto-u.ac.jp

Makoto Ohsaki

Department of Architecture and Architectural Engineering,
Graduate School of Engineering, Kyoto University, Kyoto-
Daigaku Katsura, Nishikyo, Kyoto 615-8540, Japan
E-mail: ohsaki@archi.kyoto-u.ac.jp

Methods for identifying the material parameters fall into two main classes: probabilistic (Marwala and Sibisi, 2005; Rappel et al., 2019; Rosić et al., 2013) and deterministic (Carreño et al., 2020; de Carvalho et al., 2011; Do and Ohsaki, 2022a; Hartloper et al., 2021; Jekel et al., 2019; Johansson et al., 2006; Ohsaki et al., 2016) approaches, which belong to the functional analytic and statistical regularization methods (Arridge et al., 2019), respectively. The probabilistic approach uses Bayesian inference to handle uncertainty in the parameters and observational noise (Beck and Katafygiotis, 1998; Rappel et al., 2019). It specifies a prior probability density function (PDF) for the parameters and constructs a likelihood function as the joint density function of the experimental measures for given parameter values. Parameter uncertainty and observational noise are incorporated in the prior PDF and likelihood function, respectively. To handle a costly likelihood function, a rejection sampler of the approximate Bayesian computation can be used (Turner and Zandt, 2012). Having the prior PDF and the likelihood function, Bayes' rule with support from a posterior sampling technique, for example, the Metropolis algorithm (Tarantola, 2005), generates posterior samples for the parameters. From these samples, the posterior estimates of the parameters, such as mean, variance, and maximum a posteriori (MAP), can be found and further used for other analyses or uncertainty propagation. A drawback of the probabilistic approach is that it may lead the parameter identification to a wrong direction if the prior PDF is not selected properly. Nevertheless, it does not specify how to select a proper prior PDF. The approach also seems not familiar to practicing structural engineers who are still hesitant to perform sophisticated probabilistic computations.

In contrast to the probabilistic approach, the deterministic approach seeks a deterministic estimate of each parameter by using an optimization algorithm to minimize an error function that represents the difference between the simulated and measured responses of interest. It works on the assumption that uncertainty in the parameters can be neglected while observational noise is normally distributed with zero mean. The deterministic approach is indeed a special case of the probabilistic approach when a constant and the MAP point are used as the prior PDF and the optimal parameter vector, respectively. Depending on the characteristic of the inverse problem, for example, continuous or discrete, or cheap-to-solve or expensive-to-solve, the associated optimization algorithm is selected accordingly, which can be one of the conventional optimization algorithms such as population-based (Mahmoudi et al., 2011), gradient-based (de Carvalho et al., 2011), or hy-

brid algorithms (Chaparro et al., 2008). A comparative evaluation of such algorithms for parameter identification in large kinetic models can be found in Villaverde et al. (2018). Furthermore, since modeling the cyclic elastoplastic behavior of structural steels demands a substantial computational cost, the deterministic approach commonly limits itself to identification problems formulated for uniaxial cyclic tests with few loading cycles that, in turn, facilitate the use of any optimization algorithm. Therefore, it is desirable to extend the applications of the deterministic approach to complex identification problems, for example, when multiaxial cyclic behavior of the material or long period cyclic loading is of interest. Accordingly, the computational cost due to the calculation of the error functions should be taken into consideration.

Inverse problems are ill-posed as their solutions depend on the experimental data of interest (Arridge et al., 2019). A small change in the data used for identification may lead to large errors in the resulting parameters as well as their prediction performance, which we call the dataset-specific bias. The effect of such bias on the identification results, however, is not fully explored by the methods of using conventional optimization algorithms, which simply calibrate the parameters based on experimental measures from a single loading history. Consequently, the dataset-specific bias may lead the resulting parameters to inaccurate predictions of material behavior under other loading histories (Do and Ohsaki, 2022a). When different loading histories are available, different sets of identified parameters are found by solving independent parameter identification problems. This motivates an investigation of possibility of simultaneously incorporating multiple sets of experimental measures from different loading histories into one parameter identification problem, which, as expected, can mitigate the data-specific bias.

Standard Bayesian optimization (BO) (Frazier, 2018; Jones et al., 1998; Shahriari et al., 2016; Snoek et al., 2012) is a sequential sampling technique for solving a bound-constrained optimization problem having an expensive-to-evaluate objective function, which is often evaluated through a costly simulation. BO generates a dataset of the objective values for a small number of design variable sets (or parameter sets). This dataset is then used for selecting a best-observed solution as well as for constructing a Gaussian process (GP) model (Rasmussen and Williams, 2006) that probabilistically describes the relation between the objective function and the design variables. The best-observed solution and the GP model enable BO to formulate an acquisition function that specifies a good, new design point for the next BO iteration without calling any simula-

tion, thereby reducing the number of simulation calls considerably. This is brought by a remarkable ability of the acquisition function to balance exploitation, i.e., improving the best-observed solution in its neighborhood, and exploration, i.e., searching the design space regions where uncertainty in GP predictions is large. Following the success of the standard BO, various BO variants have been proposed for solving constrained single- and multi-objective optimization problems (Feliot et al., 2017). In material and structural engineering designs, BO finds its successful applications to designing materials with mixed quantitative and qualitative variables (Zhang et al., 2020), optimizing auxetic (Tran et al., 2019) and architected materials (Vangelatos et al., 2021), handling structural optimization problems (Do et al., 2021; Mathern et al., 2021), and identifying material parameters for multiscale crystal plasticity models (Kuhn et al., 2021) and for steels under cyclic loadings (Do and Ohsaki, 2022a).

As a continuation of our recent work on the identification of elastoplastic constitutive parameters using the standard BO (Do and Ohsaki, 2022a), this study introduces a multi-objective inverse problem to finding a set of compromise elastoplastic parameters for structural steels subjected to various cyclic loadings. We simultaneously minimize the error functions that represent the differences between the simulated responses associated with the loadings of interest and those measured experimentally. By doing so, we aim to mitigate the unfavorable effect of the dataset-specific bias on the prediction performance of identified parameters, which is observed in Do and Ohsaki (2022a). Proximal-exploration multi-objective BO (MOBO) is then proposed for solving the multi-objective inverse problem. MOBO sorts an initial approximate Pareto front of parameters from a dataset generated for a small number of different samples of parameters and the corresponding error function values. It then relies on the hypervolume measure of the current Pareto front, the GP models, and an exploration surrounding the current best compromise solution (i.e., proximal exploration) to formulate an acquisition function that intelligently guides the improvement of the approximate Pareto front. Related MOBO algorithms and proximal-exploration strategies can be found in Daulton et al. (2021); Do et al. (2021); Mathern et al. (2021); Roussel et al. (2021). Once implemented, MOBO offers the best-found Pareto front of parameters to the identification problem, which allows designers to specify a set of material parameters for their design in a flexible way. Nevertheless, we will show that the best compromise solution on the obtained Pareto front can be used for structural response predictions.

The remainder of this paper is composed as follows. Section 2 briefly describes the nonlinear combined isotropic/kinematic hardening model for simulating the cyclic behavior of structural steels. The multi-objective inverse problem is then formulated. Section 3 details the proposed MOBO for solving the formulated multi-objective inverse problem. Performance of MOBO is verified against a simple bi-objective minimization problem in Section 4. Section 5 uses MOBO for identifying the material parameters for a steel specimen and a bi-material cantilever. It also demonstrates how the parameters obtained from solving the multi-objective inverse problem can reduce the dataset-specific bias. Section 6 provides conclusions. Mathematical foundation of the GP model is provided in Appendix.

2 Multi-objective inverse problem for parameter identification

2.1 Nonlinear combined isotropic/kinematic hardening model

The cyclic constitutive model of structural steel describes the relationship between the strain and stress states of the material at each time instant when subjected to cyclic loading. This relationship is established from the steel status that is either elastic or plastic and can be detected by the following von Mises yield condition:

$$F = \|\boldsymbol{\xi}\| - \sqrt{\frac{2}{3}}\sigma_y \leq 0 \quad (1)$$

where $\boldsymbol{\xi} = \text{dev}[\boldsymbol{\sigma}] - \text{dev}[\boldsymbol{\alpha}]$ the shifted-stress tensor; $\text{dev}[\boldsymbol{\sigma}]$ the deviatoric part of $\boldsymbol{\sigma}$; $\|\cdot\|$ the 2-norm of the tensor; $\boldsymbol{\sigma}$ the stress tensor at a point of a steel body; $\boldsymbol{\alpha}$ the back-stress tensor; and σ_y the yield stress.

Solid mechanics often uses isotropic and kinematic hardening models for describing the strain hardening process of structural steel subjected to cyclic loading. In the isotropic hardening model, the yield surface $F = 0$ increases its size during the evolution of plastic deformations, while its shape and the location of its center are fixed. As a result, $\boldsymbol{\alpha}$ does not appear in Eq. (1), leading the yield surface to be an isotropic function of stress, which cannot capture the Bauschinger effect (Lemaitre and Chaboche, 1994). Since structural steel exhibits a saturation point of stress at a large deformation, the isotropic hardening model can describe the increment of size of the yield surface using the following monotonically increasing nonlinear function (Voce, 1948):

$$\sigma_y = \sigma_{y,0} + Q_\infty [1 - \exp(-b\epsilon_{\text{eq}}^p)] \quad (2)$$

where $\sigma_{y,0}$ denotes the initial yield stress; Q_∞ the difference of the stress saturation and $\sigma_{y,0}$; b the isotropic saturation rate; and $\dot{\epsilon}_{\text{eq}}^{\text{p}}$ the current equivalent plastic strain determined based on its previous state and the rate $\dot{\epsilon}_{\text{eq}}^{\text{p}}$.

The kinematic hardening model, on the other hand, does not change the size and shape of the yield surface during its evolution process. Instead, the center of the yield surface, i.e., $\boldsymbol{\alpha}$, is updated through a rigid translation in the evolution direction of the plastic strain. This enables the kinematic hardening model to capture the Bauschinger effect. For a better approximation, $\boldsymbol{\alpha}$ can be further decomposed into n_k components as (Chaboche and Rousselier, 1983)

$$\boldsymbol{\alpha} = \sum_{k=1}^{n_k} \boldsymbol{\alpha}_k \quad (3)$$

where the rate of $\boldsymbol{\alpha}_k$ can be described by a nonlinear kinematic hardening rule as (Armstrong and Frederick, 1966)

$$\dot{\boldsymbol{\alpha}}_k = \sqrt{\frac{2}{3}} C_k \dot{\epsilon}_{\text{eq}}^{\text{p}} \mathbf{n} - \gamma_k \dot{\epsilon}_{\text{eq}}^{\text{p}} \boldsymbol{\alpha}_k \quad (4)$$

where $\mathbf{n} = \boldsymbol{\xi}/\|\boldsymbol{\xi}\|$ the unit normal vector of the yield surface; and C_k and γ_k the translation and relaxation rates of $\boldsymbol{\alpha}_k$, respectively.

The nonlinear combined isotropic/kinematic hardening model was developed with Eqs. (2) and (4) for simultaneous use of properties of isotropic and nonlinear kinematic hardening. Let $\mathbf{x} = [x_1, \dots, x_n] \in \mathbb{R}^n$ denote the vector of n material parameters for such a hardening model. Thus, $\mathbf{x} = [E, Q_\infty, b, \sigma_{y,0}, C_1, \gamma_1]$ if we use one back-stress component in Eq. (3) and a fixed Poisson's ratio, where E is Young's modulus of the material.

2.2 Multi-objective inverse problem for parameter identification

Recall that the cyclic elastoplastic behavior depends on loading conditions (Paul et al., 2011), leading the parameters identified from a single loading history to be biased and giving inaccurate predictions of structural behavior under other loading histories. It is important to take into account this dataset-specific bias when selecting a set of material parameters for a seismic design because the characteristics of potential earthquakes are unpredictable. If the experimental measures from different loading histories are available for use in parameter identification, the data-set specific bias may be reduced and the resulting parameters become more reliable (Do and Ohsaki, 2022a).

Let $f_i(\mathbf{x}): \mathbb{R}^n \rightarrow \mathbb{R}$ denote the i th error function that represents the difference between the i th structural response of interest simulated from a numerical model of the i th experiment, characterized by \mathbf{x} , and the corresponding measured response. When the material (or structural component) is tested under a total of I different cyclic loading histories, the optimal \mathbf{x} can be identified by simultaneously minimizing the corresponding I error functions, namely, $f_1(\mathbf{x}), \dots, f_I(\mathbf{x})$. Here, $f_i(\mathbf{x})$ is formulated from the response associated with the i th cyclic loading history, $i = \{1, \dots, I\}$. As there exists a trade-off between the minimized values of the error functions (Do and Ohsaki, 2022a), it is desirable to formulate a multi-objective minimization problem for finding the best trade-off between them. By further assuming that modeling errors are beyond the scope of this study and uncertainty in the parameters can be neglected, the optimal \mathbf{x} can be found by solving the following problem:

$$\begin{aligned} & \underset{\mathbf{x}}{\text{minimize}} && [f_1(\mathbf{x}), \dots, f_I(\mathbf{x})] \\ & \text{subject to} && \mathbf{x} \in [\mathbf{x}_l, \mathbf{x}_u] \end{aligned} \quad (5)$$

where \mathbf{x}_l and \mathbf{x}_u are the specified lower and upper bounds of \mathbf{x} , respectively.

Let $d_{i,t}^{\text{s}}$ denote the simulated value of the response of interest at the t th time step of the i th cyclic loading history of N_i discrete steps, and $d_{i,t}^{\text{m}}$ represent the corresponding measured value. Following the root-mean-square deviation, $f_i(\mathbf{x})$ is formulated as (Ohsaki et al., 2016)

$$f_i(\mathbf{x}) = \sqrt{\frac{1}{N_i} \sum_{t=1}^{N_i} (d_{i,t}^{\text{s}}(\mathbf{x}) - d_{i,t}^{\text{m}})^2} \quad (6)$$

A common approach to finding Pareto-optimal (or compromise) solutions to multi-objective optimization problems is to use population-based algorithms, for example, the non-dominated sorting genetic algorithm II (NSGA-II) (Deb et al., 2002). These algorithms directly evaluate the objective functions for all individuals of a population. Unfortunately, it is too costly to use them for solving problem (5) because direct evaluation of $f_i(\mathbf{x})$ for all individuals of the population demands a substantial computational cost for calculating $d_{i,t}^{\text{s}}(\mathbf{x})$. To solve the problem effectively, we propose proximal-exploration MOBO in the next section. As all the error functions $f_i(\mathbf{x})$ are treated equally, we drop the subscript hereafter to simplify the exposition.

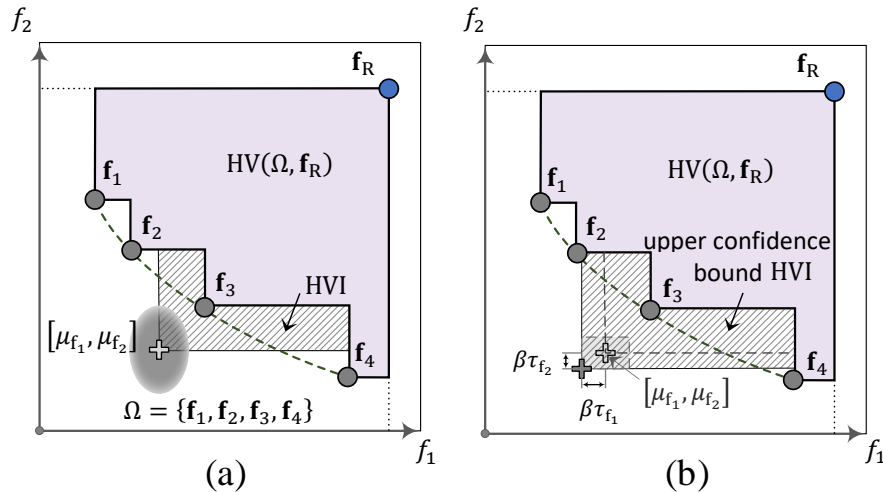


Fig. 1: Examples of the expected and upper bound HVI values for a bi-objective minimization problem. (a) Expected HVI ; (b) Upper confidence bound HVI.

3 Parameter identification using proximal-exploration multi-objective Bayesian optimization

3.1 Proximal-exploration multi-objective Bayesian optimization

The proposed MOBO starts by generating a training dataset $\mathcal{D} = \{\mathbf{x}_k, f_k\}_{k=1}^N$, where $\mathbf{x}_k \in \mathbb{R}^n$ is a vector of material parameters, and $f_k \in \mathbb{R}$ the value of f at \mathbf{x}_k . The samples \mathbf{x}_k are randomly generated using Latin-hypercube sampling (Santner et al., 2018). The number of initial samples is problem-dependent, which is recommended as $N = 10n$ (Do and Ohsaki, 2022a). To evaluate f_k , the nonlinear combined isotropic/kinematic hardening incorporated in the FE model of the experiment evaluates $d_{i,t}^s$ in Eq. (6) using \mathbf{x}_k as the input of material properties for the i th loading history used in the cyclic test. From the members of \mathcal{D} , MOBO finds a set of approximate Pareto-optimal solutions to problem (5) using a non-dominated sorting algorithm (Tom, 2019) and sequentially improves this set until it can no longer be improved or until the budgeted computational cost has been reached.

Let $\Omega = \{\mathbf{f}_1, \dots, \mathbf{f}_M\} \in \mathbb{R}^I$ be the set of M approximate Pareto-optimal solutions sorted from \mathcal{D} . The improvement of Ω performs the following five steps: (1) construct a total of I GP models as surrogates for the error functions; (2) find the best compromise solution from the members of Ω using a fuzzy-based method; (3) formulate the acquisition function based on the current GP models, Ω , and the current best compromise solution; (4) maximize the formulated acquisition function for updating \mathcal{D} ; and (5) sort new Pareto-optimal so-

lutions from the updated \mathcal{D} and reiterate from (1) if MOBO is still in process.

In the first step of solution improvement, MOBO uses the DACE toolbox (Lophaven et al., 2002) to construct a GP model that approximates the error function $f(\mathbf{x}) \in \{f_1(\mathbf{x}), \dots, f_I(\mathbf{x})\}$. By conditioning a Gaussian probability distribution over possible regression functions on \mathcal{D} , the GP model describes the relation between f and \mathbf{x} , denoted as $\hat{f}(\mathbf{x})$, using a conditional Gaussian. Detailed derivations of this conditional Gaussian are provided in Appendix. Following Eq. (A.7), the GP prediction of the error function at a particular \mathbf{x} reads

$$\hat{f}(\mathbf{x}) \sim \mathcal{N}(\mu_f(\mathbf{x}), \tau_f^2(\mathbf{x})) \quad (7)$$

where \mathcal{N} denotes a univariate Gaussian; and $\mu_f(\mathbf{x})$ and $\tau_f(\mathbf{x})$ the mean and standard deviation of $\hat{f}(\mathbf{x})$, respectively. Eq. (7) probabilistically maps the parameter space onto the error function space.

The second step for improving Ω is to find its best compromise member, or equivalently, the best compromise solution of parameters, denoted as \mathbf{x}_0 . This can be done using the fuzzy-based method that computes the following membership function for the i th error function of each member of Ω (Abido, 2003):

$$m_{i,j} = \begin{cases} 1 & \text{if } f_{i,j} = f_i^{\min} \\ \frac{f_i^{\max} - f_{i,j}}{f_i^{\max} - f_i^{\min}} & \text{if } f_i^{\min} < f_{i,j} < f_i^{\max}, i = 1, \dots, I \\ 0 & \text{if } f_{i,j} = f_i^{\max} \end{cases} \quad (8)$$

where j indicates the j th solution among M members of Ω ; $f_{i,j}$ the i th error function value of the j th solution;

and f_i^{\min} and f_i^{\max} the minimum and maximum values among M values of the i th error function, respectively. Subsequently, a normalized membership function corresponding to $m_{i,j}$ reads

$$m_j = \frac{\sum_{i=1}^I m_{i,j}}{M \sum_{i=1}^I m_{i,j}} \quad (9)$$

The best compromise solution \mathbf{x}_0 corresponds to a member of Ω that has the largest value of the normalized membership function m_j . If Ω has only two members, either can be selected. Also, the second-best compromise solution, which is used in Section 5, has the second-largest value of m_j .

The third step for improving Ω is to formulate a hypervolume-based acquisition function that intelligently guides MOBO (Do and Ohsaki, 2022b; Do et al., 2021). This formulation is natural because (1) the acquisition function, a key ingredient of BO, directs the algorithm toward better solutions by mapping our belief about an improvement in the current solutions to a measure of how promising each parameter vector in the parameter space is if it is specified in the next optimization iteration; and (2) the hypervolume (HV) measure is often used in the field of multi-objective design to assess the quality of different sets of solutions (Emmerich et al., 2006). Let $\mathbf{f}_R \in \mathbb{R}^I$ denote a fixed reference point in the error function space so that it is dominated by all members of Ω . Each element of \mathbf{f}_R can be assigned a sufficiently large value of the corresponding error function at which the prediction error is unacceptable. As an example, Fig. 1 shows the HV defined by a set of four Pareto-optimal solutions to a bi-objective minimization problem and a reference point dominated by these solutions. Mathematically, the HV of Ω is a Lebesgue measure of the I -dimensional subspace dominated by Ω and bounded above by \mathbf{f}_R , such that

$$\text{HV}(\Omega, \mathbf{f}_R) = \Lambda(\{\mathbf{f} \in \mathbb{R}^I \mid \exists \mathbf{f}_j \in \Omega : \mathbf{f}_j \preceq \mathbf{f} \text{ and } \mathbf{f} \preceq \mathbf{f}_R\}) \quad (10)$$

where $\Lambda(\cdot)$ denotes the Lebesgue measure defined for a set on \mathbb{R}^I as the I -dimensional volume of this set, for example, $\Lambda(\cdot)$ is equivalent to the standard measure of length, area, or volume of set (\cdot) if $I = 1, 2, \text{ or } 3$, respectively; \mathbf{f} a point in the error function space; and $\mathbf{f}_j \preceq \mathbf{f}$ indicates \mathbf{f}_j dominates \mathbf{f} . The HV in this study is evaluated using an algorithm developed by Fonseca et al. (2006).

Now suppose MOBO is processing its s th iteration and has to specify a new parameter vector \mathbf{x}_{s+1} in the

next iteration (i.e., $s + 1$) at which a simulation is performed to update the current dataset \mathcal{D} as well as the current solution set Ω . Since we wish to reduce the number of simulations as much as possible, \mathbf{x}_{s+1} should be ideal in the parameter space as it maximizes the improvement of Ω . Maximizing the improvement of Ω , therefore, coincides with maximizing the difference of the HV defined by the union of $\mathbf{f}(\mathbf{x})$ and Ω , and that defined by Ω , where $\mathbf{f}(\mathbf{x})$ is evaluated at an arbitrary vector \mathbf{x} in the parameter space. This difference is further represented by the following hypervolume improvement (HVI) indicator (Do and Ohsaki, 2022b; Do et al., 2021):

$$\text{HVI}(\mathbf{f}(\mathbf{x}) \mid \Omega, \mathbf{f}_R) = \text{HV}(\mathbf{f}(\mathbf{x}) \cup \Omega, \mathbf{f}_R) - \text{HV}(\Omega, \mathbf{f}_R) \quad (11)$$

where $\mathbf{f}(\mathbf{x}) \cup \Omega$ denotes the union of $\mathbf{f}(\mathbf{x})$ and Ω .

Since the error function values are evaluated through costly simulations, it is inefficient to maximize HVI by direct evaluation of $\text{HV}(\mathbf{f}(\mathbf{x}) \cup \Omega, \mathbf{f}_R)$. Fortunately, the expected value of HVI can be estimated by integrating $\text{HV}(\mathbf{f}(\mathbf{x}) \cup \Omega, \mathbf{f}_R)$ over a non-dominated region of the error function space defined by the current Ω and the Gaussian models for the error functions (e.g., shading in Fig. 1(a)). In this way, the non-dominated region can be decomposed into a set of small disjoint cells over which the integral can be approximated using an analytical form (Couckuyt et al., 2014). However, the calculation of the expected HVI using such an integral is not advantageous for quickly finding \mathbf{x}_{s+1} (Roussel et al., 2021). Thus, we replaced $\text{HV}(\mathbf{f}(\mathbf{x}) \cup \Omega, \mathbf{f}_R)$ with $\text{HV}(\boldsymbol{\mu}_f(\mathbf{x}) \cup \Omega, \mathbf{f}_R)$ (Do and Ohsaki, 2022b; Do et al., 2021), leading to an expected measure of HVI as illustrated by the hatched area in Fig. 1(a), where $\boldsymbol{\mu}_f(\mathbf{x})$ is the Gaussian mean vector of the error functions at \mathbf{x} given in Eqs. (7) and (A.8). The reason for this replacement is that it is often more computationally efficient to perform more optimization iterations than to do an exact calculation of HVI at each iteration. Roussel et al. (2021) further enhanced exploration ability of MOBO using $\text{HV}(\boldsymbol{\mu}_f(\mathbf{x}) - \beta \boldsymbol{\tau}_f(\mathbf{x}) \cup \Omega, \mathbf{f}_R)$ for defining an upper confidence bound HVI, as shown by the hatched area in Fig. 1(b), where $\boldsymbol{\tau}_f(\mathbf{x})$ is the Gaussian standard deviation vector of the error functions at \mathbf{x} given in Eqs. (7) and (A.9), and β a positive scalar that controls the trade-off between exploration and exploitation of MOBO. A large value of β prioritizes MOBO exploration. Here, the upper confidence bound HVI is an extension of the GP-upper confidence bound criterion, which is an acquisition function for solving single-objective optimization problems (Srinivas et al., 2010).

As we aim to use the best compromise solution \mathbf{x}_0 of identified material parameters for structural response

predictions, we bias MOBO exploration toward the non-dominated region surrounding the best compromise member of Ω and multiply the upper confidence bound HVI by an exponential function of $-\frac{1}{2}\|\mathbf{x}_n - \mathbf{x}_{0n}\|$, where \mathbf{x}_n and \mathbf{x}_{0n} are normalized values of \mathbf{x} and \mathbf{x}_0 , respectively. This is to address the selection of an efficient set of material parameters after having the Pareto solutions, and is inspired by two previous exploration schemes. The first exploration scheme by [Daulton et al. \(2021\)](#) focused on a trust region (in the error function space) surrounding a member of Ω that has maximum HV contribution. The second exploration scheme by [Roussel et al. \(2021\)](#) carried out exploration in the neighborhood of the most recently observed point (in the parameter space) for minimizing the traveling distance by the optimization steps. As mentioned above, we formulate the following acquisition function to specify \mathbf{x}_{s+1} :

$$\alpha(\mathbf{x}) = \text{HVI}(\boldsymbol{\mu}_f(\mathbf{x}) - \beta\boldsymbol{\tau}_f(\mathbf{x}) | \Omega, \mathbf{f}_R) \exp\left(-\frac{1}{2}\|\mathbf{x}_n - \mathbf{x}_{0n}\|\right) \quad (12)$$

Here \mathbf{x}_n and \mathbf{x}_{0n} are the normalized values to prevent dependence of the exponential function value on the parameter units. The components of \mathbf{x}_n and \mathbf{x}_{0n} are derived from the corresponding components of \mathbf{x} , \mathbf{x}_0 , \mathbf{x}_l , and \mathbf{x}_u as

$$x_n = \frac{x - x_l}{x_u - x_l}; \quad x_{0n} = \frac{x_0 - x_l}{x_u - x_l} \quad (13)$$

Thus, the next parameter vector \mathbf{x}_{s+1} can be found by solving

$$\begin{aligned} \mathbf{x}_{s+1} = \operatorname{argmax}_{\mathbf{x}} \quad & \alpha(\mathbf{x}) \\ \text{subject to} \quad & \mathbf{x} \in [\mathbf{x}_l, \mathbf{x}_u] \end{aligned} \quad (14)$$

The exponential in Eq. (12) measures the similarity between \mathbf{x} and \mathbf{x}_0 . Thus, when multiplying HVI by this exponential, we are likely to find \mathbf{x}_{s+1} in the neighborhood of \mathbf{x}_0 which, as expected, can have the most contribution to the improvement in the current HV of Ω . Such an exploration is referred to as proximal exploration. It can also make the improvement of HV more stable than that observed when using only HVI to guide MOBO ([Do and Ohsaki, 2022b](#)). Moreover, although $\mathbf{x} = \mathbf{x}_0$ maximizes the exponential, we do not reselect \mathbf{x}_0 because the HVI at \mathbf{x}_0 equals zero. It is worth noting that it is not necessary to restrict \mathbf{x}_{s+1} to the neighborhood of \mathbf{x}_0 because a new parameter vector that is far from \mathbf{x}_0 can also be selected if it provides a large value of HVI.

The fourth step for improving Ω is to solve problem (14) using an appropriate optimization algorithm.

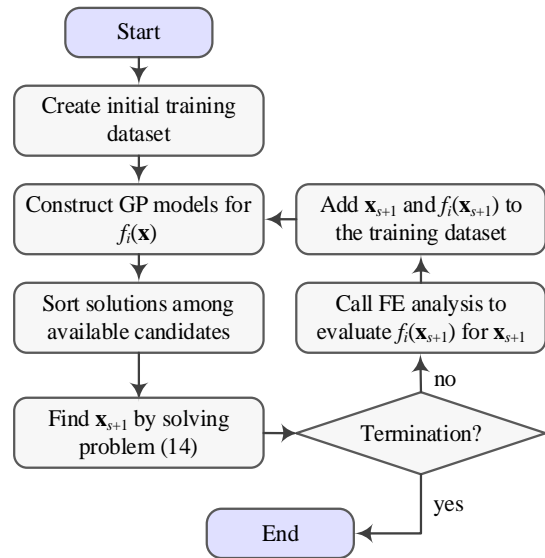


Fig. 2: Proposed MOBO for parameter identification.

Such an algorithm should avoid using the gradient information of $\alpha(\mathbf{x})$ for finding the search direction because it is difficult to evaluate the gradient of the upper confidence bound HVI in Eq. (12). Thus, a population-based method (e.g., genetic algorithm (GA)), a direct method (e.g., pattern search), or a stochastic method (e.g., simulated annealing) can be a viable choice.

With \mathbf{x}_{s+1} , MOBO terminates if it satisfies one of the following stopping conditions: (1) the number of iterations reaches a pre-specified upper limit, and (2) \mathbf{x}_{s+1} is identical to any available sample of parameters in \mathcal{D} . Otherwise, MOBO updates \mathcal{D} and starts a new iteration.

3.2 Identification procedure

Fig. 2 summarizes the identification procedure using the proposed MOBO. We implement the following seven steps:

- Step (0): Randomly generate initial samples of \mathbf{x} using Latin-hypercube sampling. Create \mathcal{D} by performing FE analyses for the generated samples. Find Ω from \mathcal{D} .
- Step (1): Based on \mathcal{D} , construct GP models for the error functions; see Appendix.
- Step (2): Find \mathbf{x}_0 associated with the best compromise member of Ω using Eqs. (8) and (9).
- Step (3): Formulate $\alpha(\mathbf{x})$; see Eq. (12).
- Step (4): Find \mathbf{x}_{s+1} by performing proximal exploration surrounding \mathbf{x}_0 , or equivalently, solving problem (14).

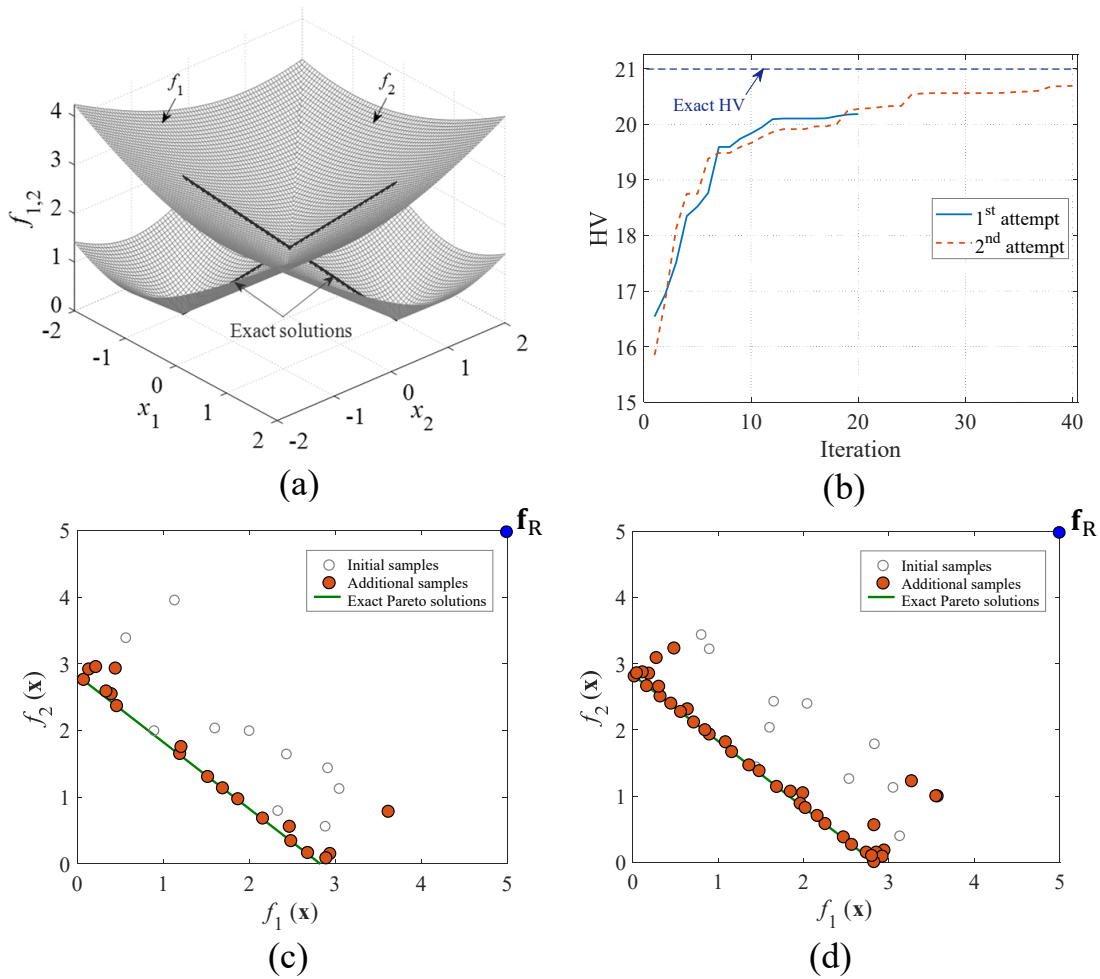


Fig. 3: MOBO for solving problem (15). (a) Surfaces of two objective functions and the exact solutions; (b) Histories of HVs for two MOBO attempts; (c) Initial and additional design points for the first MOBO attempt; (d) Initial and additional design points for the second MOBO attempt.

- Step (5): Terminate the identification process and output the approximate Pareto-optimal parameters if one of the mentioned stopping conditions is met. The best compromise solution \mathbf{x}_0 on the final Pareto front may be used for prediction of structural responses. Otherwise, proceed to Step (6).
- Step (6): Evaluate the error function values corresponding to \mathbf{x}_{s+1} by calling the FE analyses, update \mathcal{D} as well as Ω , and reiterate from Step (1).

4 Test problem

Before being used for parameter identification, the performance of MOBO is verified against a bi-objective minimization problem. The problem is stated as (Rous-

sel et al., 2021)

$$\begin{aligned} & \underset{\mathbf{x}}{\text{minimize}} && [f_1(\mathbf{x}), f_2(\mathbf{x})] \\ & \text{subject to} && x_i \in [-2, 2], i = 1, 2 \end{aligned} \quad (15)$$

where

$$f_1(\mathbf{x}) = \|\mathbf{x} - \mathbf{1}\|; \quad f_2(\mathbf{x}) = \|\mathbf{x} + \mathbf{1}\| \quad (16)$$

Fig. 3(a) shows the exact Pareto-optimal solutions to problem (15). Their image in the objective function space is the line segment connecting $[f_1, f_2] = [0, 2\sqrt{2}]$ and $[2\sqrt{2}, 0]$, as illustrated in Fig. 3(c).

We perform MOBO two times, each starts with a random set of ten sampling points. The numbers of iterations for the first and second MOBO attempts are limited at 20 and 40, respectively. The assigned reference point $\mathbf{f}_R = [5, 5]$ leads to an exact HV of 21 (i.e., $5 \times 5 - 0.5 \times 2\sqrt{2} \times 2\sqrt{2}$). Problem (14) is solved in

Table 1: Parameters for GA.

Parameter	Value
Population size	200
Maximum number of generations	50
Crossover fraction	65%
Elite transfer	2
Fitness function tolerance	10^{-12}

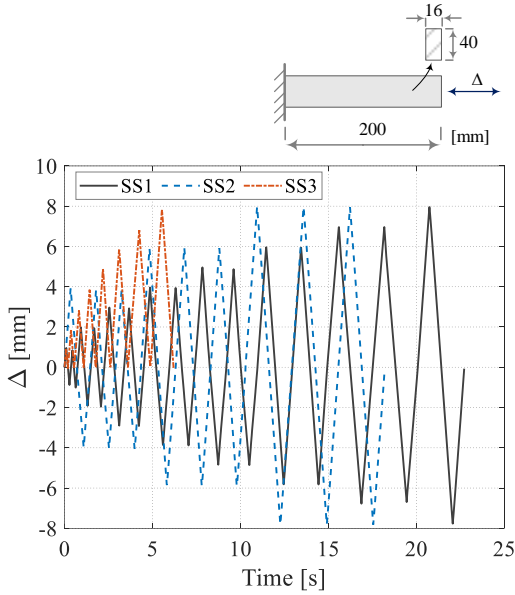


Fig. 4: Steel specimen and three loading histories for cyclic tests (Do and Ohsaki, 2022a; Yamada and Jiao, 2016).

each iteration of MOBO using GA, whose parameters are listed in Table 1. The parameter β in Eq. (12) is assigned as 0.01 since we focus on MOBO exploitation for improving HV. The effect of β on the convergence speed of MOBO may be of interest when fixing the initial dataset; however, this is not our focus here. The HV and additional sampling point after each MOBO iteration are recorded.

Fig. 3(b) confirms that the HV values during the two MOBO attempts increase as much as possible and tend to converge to the exact HV when increasing the number of MOBO iterations. As a result, the additional sampling points by MOBO, as shown in Figs. 3(c) and (d), well capture the exact solutions. These results indicate a good performance of the proposed MOBO in solving problem (15).

5 Identification examples

5.1 Parameters for a steel specimen

The elastoplastic parameters are identified to simulate the uniaxial cyclic behavior of a steel specimen in Fig. 4, which was used in our previous works on single-objective inverse problems (Do and Ohsaki, 2022a; Ohsaki et al., 2016). The specimen was tested under three different static cyclic loading histories SS1, SS2, and SS3 by Yamada and Jiao (2016).

The axial force and corresponding axial deformation of the specimen were measured in the static cyclic tests. Time in the horizontal axis of Fig. 4 refers to a loading path parameter of each test. The measured axial force and deformation values were used for calculation of the engineering stress σ_e and the engineering strain ϵ_e at every time instant of interest, respectively. More specifically, σ_e was calculated by dividing the measured axial force by the initial cross-sectional area of the specimen while ϵ_e was evaluated by dividing the axial deformation of the specimen by its initial length. The true stress σ and the true strain ϵ were derived from σ_e and ϵ_e as

$$\sigma = (1 + \epsilon_e)\sigma_e \quad (17)$$

$$\epsilon = \ln(1 + \epsilon_e) \quad (18)$$

Test results for the specimen, therefore, consist of three experimental datasets of σ and ϵ corresponding to the three loading histories.

For identification, Young's modulus of the specimen is kept constant at $E = 205.94$ GPa, which is calibrated from the results of monotonic tension tests (Yamada and Jiao, 2016). Poisson's ratio of the specimen steel is 0.3. Thus, there are five parameters to be identified for the specimen, i.e., $\mathbf{x} = [Q_\infty, b, \sigma_{y,0}, C_1, \gamma_1]$. The interval associated with each parameter, as listed in Table 2, is taken from Do and Ohsaki (2022a). Note that the monotonic tension tests facilitate the determination of interval for $\sigma_{y,0}$.

Table 2: Material parameter intervals for the specimen.

Parameter	Lower bound	Upper bound
E [GPa]	205.94	—
$\sigma_{y,0}$ [MPa]	250	260
Q_∞ [MPa]	10	100
b	5	25
C_1 [MPa]	2000	8000
γ_1	10	100

To investigate the effect of experimental datasets used for identification on the resulting parameters as well as their prediction performance, we classify the

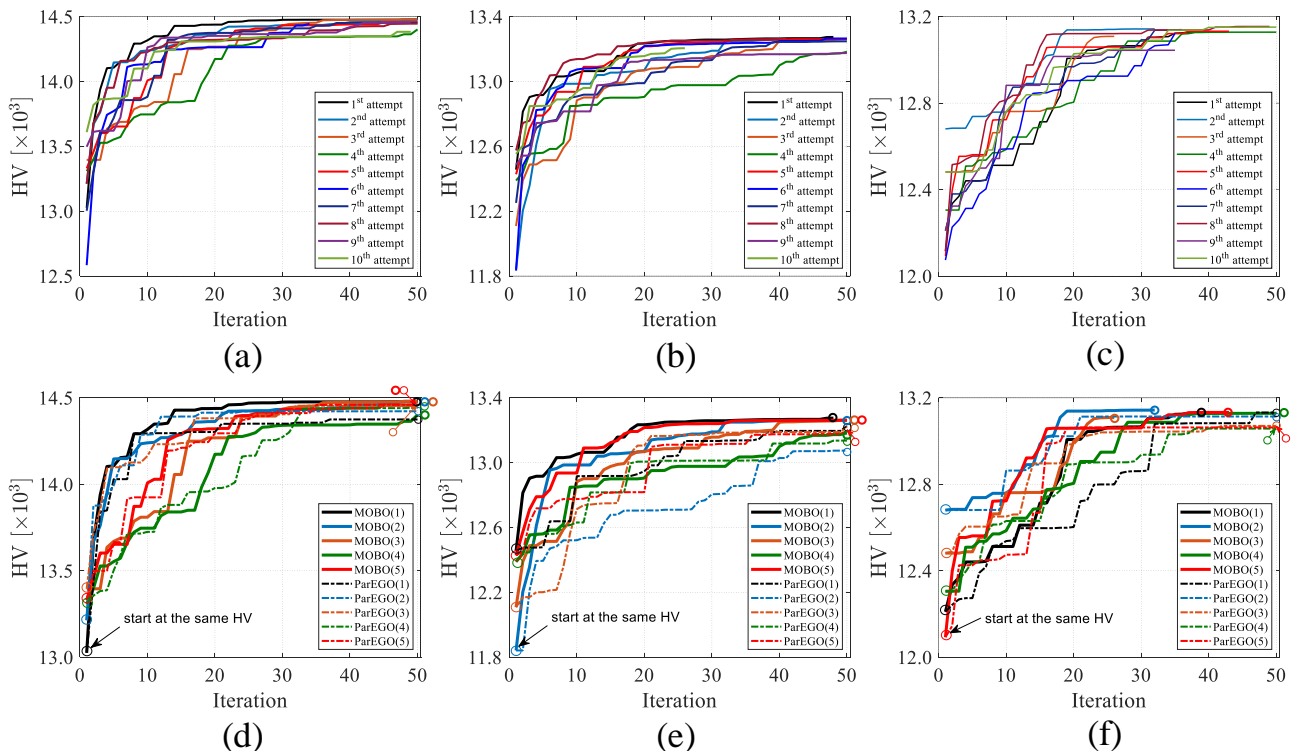


Fig. 5: Histories of HVs for different groups of experimental datasets from cyclic tests of the specimen. (a) Ten MOBO attempts, group 1; (b) Ten MOBO attempts, group 2; (c) Ten MOBO attempts, group 3; (d) The first five MOBO attempts and five ParEGO attempts, group 1; (e) The first five MOBO attempts and five ParEGO attempts, group 2; (f) The first five MOBO attempts and five ParEGO attempts, group 3.

three experimental datasets into three groups, namely, groups 1, 2, and 3, which correspond to SS1 & SS2, SS2 & SS3, and SS3 & SS1, respectively. For each group, problem (5) is formulated with two objectives that are the error functions evaluated using Eq. (6) for the measured and simulated $\sigma - \epsilon$ curves of the two individual tests. To further examine the robustness of MOBO, ten different training datasets are generated for each group. Each of these training datasets at the beginning of MOBO has 50 random samples of parameters and the corresponding error function values are evaluated by carrying out FE analyses for each sample. As a result, a total of ten Pareto fronts of material parameters are found for each group. The best Pareto front of each group corresponds to the largest HV value among ten values associated with the ten Pareto fronts. To demonstrate their prediction ability, the best and second-best compromise solutions on the best Pareto front of each group are used as input to the FE model for calculation of the error function associated with the loading history not used for identification.

As the specimen was axially loaded during the cyclic tests, it is modeled using one Abaqus linear hexahedral element with reduced integration of type C3D8R (Das-

sault Systèmes, 2017). The maximum increment size for each loading history is set as 0.01 s.

We limit the number of MOBO iterations at 50. Thus, the maximum number of simulations required for each MOBO attempt is 200 (i.e., 100 for generating the initial training dataset, and maximum 100 for performing MOBO iterations). The reference point and the parameter β in Eq. (12) are assigned as $\mathbf{f}_R = [150, 150]$ MPa and 0.01, respectively. We solve problem (14) in each MOBO iteration using GA with a large population size of 4000, which is to increase the chance of finding the global optimizer of the acquisition function by which the effect of the GA randomness on the MOBO performance can be reduced. Other parameters for GA are given in Table 1.

For comparison, we perform NSGA-II ten times, each treats the variables as real numbers and requires a total of 200 simulation calls (i.e., 20 individuals and five generations) for finding approximate Pareto fronts for each group. The solutions from NSGA-II are baselines to assess the quality of the Pareto fronts by MOBO. Moreover, ParEGO (Knowles, 2006), which is an extension of the single-objective efficient global optimization algorithm to solving multi-objective optimization prob-

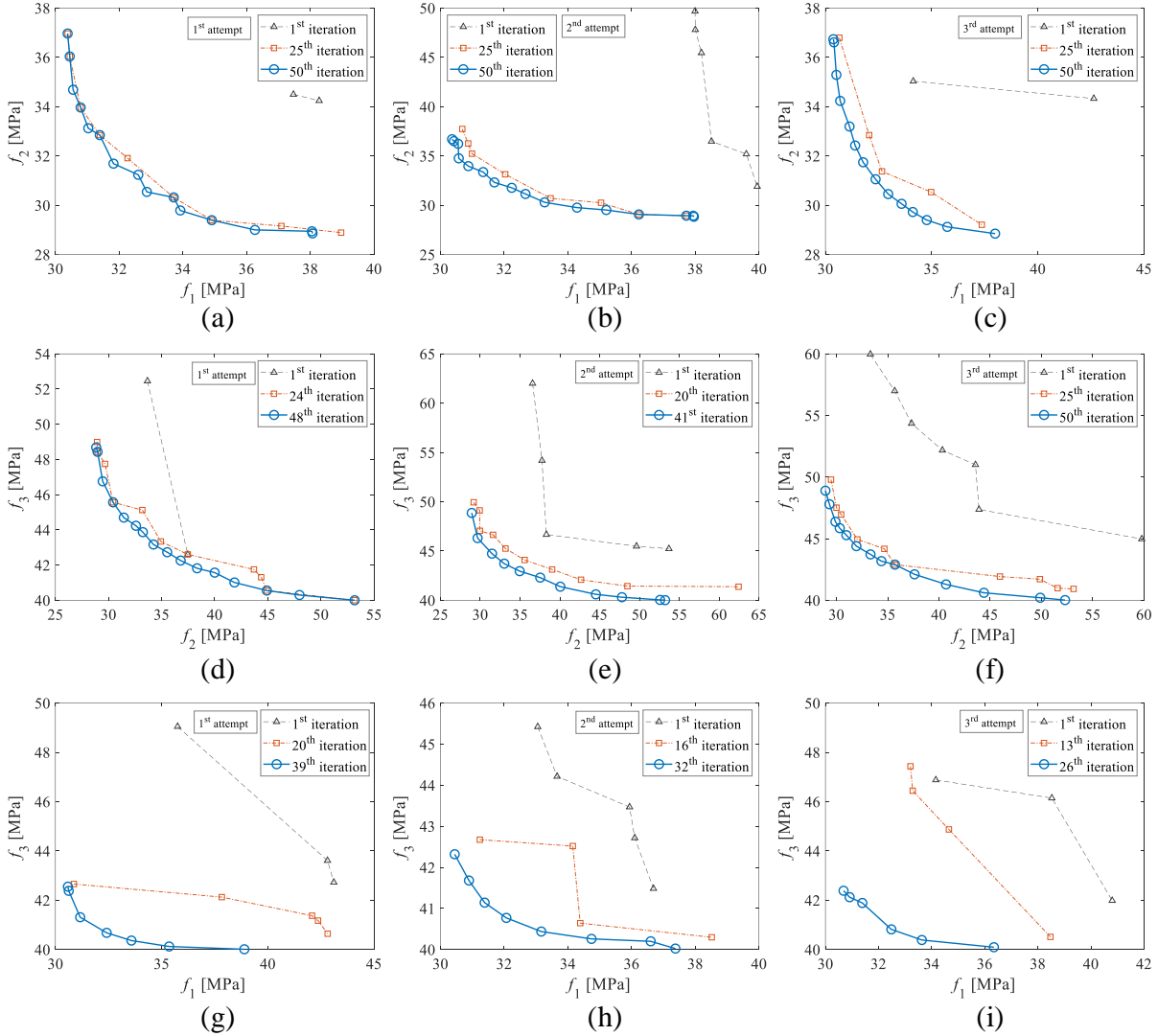


Fig. 6: Evolution of approximate Pareto-optimal solutions during the first three MOBO attempts for different groups of experimental datasets from cyclic tests of the specimen. (a), (b), (c) From group 1; (d), (e), (f) From group 2; (g), (h), (i) From group 3.

lems, is carried out five times, each characterized by 50 iterations uses the same training dataset as that at the beginning of each of the first five MOBO attempts. This is to compare the largest HV values associated with the final Pareto fronts from MOBO and ParEGO when they start at the same training dataset.

To show that the solutions to the multi-objective inverse problem of the specimen can reduce the dataset-specific bias, we compare the best and second-best compromise solutions by MOBO with those obtained by solving other six single-objective inverse problems formulated for the specimen. The first, second, or third problem, denoted as SIG 1, SIG 2, or SIG 3, respec-

tively, is formulated with single objective as the individual error of SS1, SS2, or SS3, respectively. The fourth, fifth, or sixth problem, denoted as SUM 1, SUM 2, or SUM 3, respectively, is formulated with single objective as the weighted-sum (with equal weights) error of SS1 & SS2, SS2 & SS3, or SS3 & SS1, respectively. For brevity, we use “single-objective formulation” to represent problems SIG 1, SIG 2, and SIG 3, and “weighted-sum formulation” to represent SUM 1, SUM 2, and SUM 3, even though they all have one objective. Detailed formulations of these problems and how to solve them using the standard BO can be found in [Do and Ohsaki \(2022a\)](#). Here, we only provide the identification results

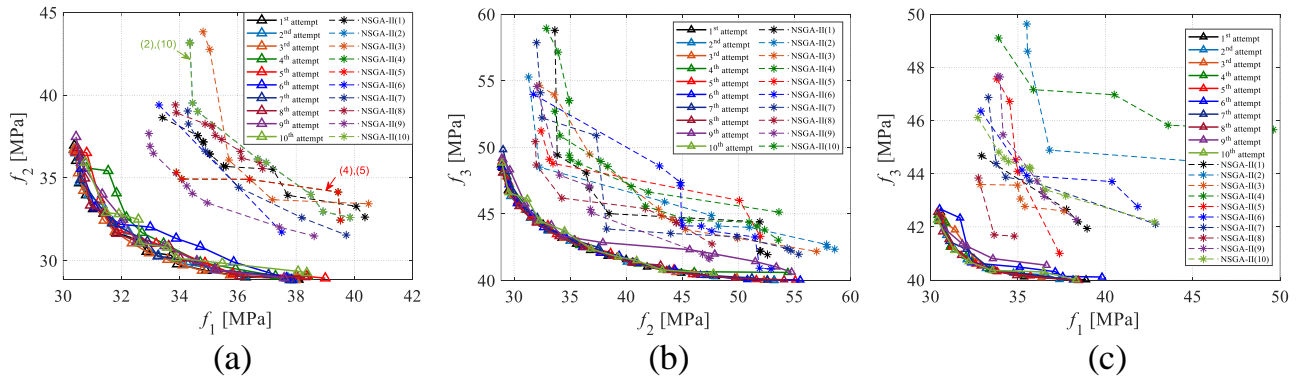


Fig. 7: Comparison of solutions by ten MOBO attempts and by ten NSGA-II attempts for different groups of experimental datasets from cyclic tests of the specimen. (a) From group 1; (b) From group 2; (c) From group 3.

obtained from solving these problems to enable a comparison with the solutions by MOBO.

Fig. 5 shows the histories of HV from the ten MOBO attempts of each group as well as the comparison between the HV histories from the first five MOBO attempts and those from the corresponding five ParEGO attempts. Although starting at different initial values, the HVs from each group tend to converge to a value as MOBO terminates. Moreover, the final HV values by most of the MOBO attempts are better than those by the ParEGO attempts when they start at the same training dataset. The optimized HV values associated with ten MOBO attempts of each group are reported in Table 3.

Table 3: Optimized HVs associated with ten MOBO attempts for different groups of experimental datasets from cyclic tests of the specimen [$\times 10^3$ (MPa) 2].

Attempt	Group 1	Group 2	Group 3
1	14.477	13.275	13.129
2	14.480	13.261	13.143
3	14.479	13.262	13.109
4	14.402	13.183	13.128
5	14.457	13.262	13.132
6	14.444	13.265	13.123
7	14.454	13.248	13.140
8	14.446	13.259	13.154
9	14.454	13.175	13.044
10	14.383	13.206	13.152

Fig. 6 illustrates the evolution of approximate Pareto optimal solutions during the first three MOBO attempts of each group. As observed, MOBO considerably improves the solution quality. Fig. 7 shows the similarity in shapes of the Pareto fronts at the last iterations of ten MOBO attempts of each group, regardless of their

difference at the very first iterations (see the first iteration along each row of Fig. 6 for the first three MOBO attempts of each group). This observation is consistent with the convergence of HV in Fig. 5. Fig. 7 also confirms that the optimization results by all MOBO attempts of each group outperform those by the corresponding ten NSGA-II attempts even though the number of simulation calls required for MOBO does not exceed that required for NSGA-II.

Table 4 provides the best (1) and second-best (2) compromise solutions on the best Pareto front of each group. It also provides the error function values associated with SS1, SS2, and SS3, namely, f_1 , f_2 , and f_3 , respectively, where the boldface value indicates the experimental dataset used for identification. The identified parameters and the corresponding error function values from SIG 1, SIG 2, SIG 3, SUM 1, SUM 2, and SUM 3 are also given (Do and Ohsaki, 2022a). As the ten Pareto fronts of each group are similar, the best and second-best compromise solutions among those on these Pareto fronts are slightly different. As observed in Table 4, there is no major difference in the values of $\sigma_{y,0}$, b , C_1 , and γ_1 for the best and second-best compromise solutions among those obtained from the three groups. However, Q_∞ is group-dependent.

Using the results in Table 4, we wish to compare the data-specific bias levels for different sets of identification results obtained from different inverse problem formulations for the specimen. Here, we consider four different sets of identification results from three problem formulations (i.e., multi-objective, single-objective, and weighted-sum formulations). The multi-objective formulation offers two sets of identification results, i.e., the best compromise and second-best compromise sets, while each of the remaining two formulations provides only one set of identification results. To enable a rig-

Table 4: Comparison of the identification results obtained from MOBO and from solving single-objective inverse problems using BO for different groups of experimental datasets of the specimen.

Group	$\sigma_{y,0}$ [MPa]	Q_∞ [MPa]	b	C_1 [MPa]	γ_1	f_1 [MPa]	f_2 [MPa]	f_3 [MPa]
1 (1)	250.373	58.208	5.058	7987.986	69.641	33.271	30.298	45.902
2 (1)	250.004	46.273	5.005	7982.653	65.429	30.861	34.236	43.168
3 (1)	250.346	39.932	5.013	7999.983	67.686	30.447	37.028	42.319
1 (2)	251.806	54.956	5.003	7855.806	68.741	32.669	31.147	45.669
2 (2)	250.005	40.323	5.025	7999.934	65.076	30.599	36.794	42.257
3 (2)	250.093	35.395	5.186	7969.030	65.229	30.895	39.244	41.680
SIG 1	250.004	42.105	5.001	7999.997	69.188	30.372	36.370	42.499
SIG 2	250.010	70.283	5.015	7999.769	70.308	37.898	28.840	48.692
SIG 3	250.008	11.939	5.000	8000.000	72.634	38.635	54.834	39.986
SUM 1	250.011	56.630	5.005	7999.996	69.096	32.627	30.732	45.261
SUM 2	250.056	57.661	5.000	8000.000	67.594	33.092	30.397	45.497
SUM 3	250.002	34.289	5.003	8000.000	67.985	30.827	40.150	41.389

orous comparison, we propose in the following a data-specific index ξ for each set of identification results.

Let $P \geq 2$ and $J \geq 2$ denote the number of parameter sets in each set of identification results and the number of tests in consideration, respectively, and $f_{j,p}$ with $j = \{1, \dots, J\}$ and $p = \{1, \dots, P\}$ indicate the j th error corresponding to the p th parameter set. Each set of identification results in Table 4, therefore, reads $J = 3$ and $P = 3$, while the best compromise set, for example, reads $f_{1,1} = \mathbf{33.271}$, $f_{1,2} = 30.861$, $f_{1,3} = \mathbf{30.447}$ MPa, and so on. For the j th test of each set of identification results, we define

$$\psi_j = f_j^{\max} - f_j^{\min}, \quad j = 1, \dots, J \quad (19)$$

where

$$\begin{aligned} f_j^{\min} &= \min\{f_{j,1}, \dots, f_{j,P}\}; \\ f_j^{\max} &= \max\{f_{j,1}, \dots, f_{j,P}\} \end{aligned} \quad (20)$$

Here f_j^{\min} , due to the data-specific bias, is a minimized value of f_j (i.e., a boldface value in Table 4). That means, f_j^{\min} is found by minimizing the error function formulated from the experimental results of test j . Meanwhile, f_j^{\max} , in most cases, corresponds to a parameter set that is found by minimizing the error function formulated from the experimental results of other tests rather than test j . For example, the set of identification results of SIG 1, SIG 2, and SIG 3 has $f_1^{\min} = \mathbf{30.372}$, $f_2^{\min} = \mathbf{28.840}$, $f_3^{\min} = \mathbf{39.986}$, $f_1^{\max} = 38.635$, $f_2^{\max} = 54.834$, and $f_3^{\max} = 48.692$ MPa. f_j^{\min} and f_j^{\max} , therefore, represent the quality of the solution to the inverse problem and its prediction performance, respectively. Thus, the larger the difference of f_j^{\max} and f_j^{\min} (i.e., ψ_j), the higher the data-specific bias level observed on the j th test. Without loss of generality, we further assume that the errors of the tests in consideration have the same unit. Normalization can be used when different units are of interest.

The following data-specific index ξ is defined for each set of identification results based on a total of J tests of consideration:

$$\xi = \frac{1}{J} \sum_{j=1}^J \psi_j \quad (21)$$

Thus, the set of identification results with the smallest value of ξ has the lowest level of dataset-specific bias.

Table 5 provides the ξ index value for each set of identification results listed in Table 4, where ψ_1 , ψ_2 , and ψ_3 are evaluated using tests SS1, SS2, and SS3, respectively. The ξ values associated with the two sets of identification results from the multi-objective formulation are better than those corresponding to the single-objective and weighted-sum formulations. The single-objective formulation shows the largest value of bias level. These results confirm that the best and second-best compromise solutions obtained from the multi-objective formulation of the inverse problem of the specimen can reduce the dataset-specific bias.

Table 5: Dataset-specific indexes for different sets of identification results evaluated using the experimental results from tests SS1, SS2, and SS3 of the specimen [MPa].

Set of results	ψ_1	ψ_2	ψ_3	ξ
Multi-objective (1)	2.823	6.730	3.583	4.379
Multi-objective (2)	2.070	8.096	3.990	4.719
Single-objective	8.263	25.994	8.706	14.321
Weighted-sum	2.265	9.418	4.109	5.264

Fig. 8 compares the measured and simulated $\sigma - \epsilon$ curves from each loading history using the best compromise solution of each group listed in Table 4 for the simulation, where the arrow at the lower right corner of the figure indicates the experimental dataset used for

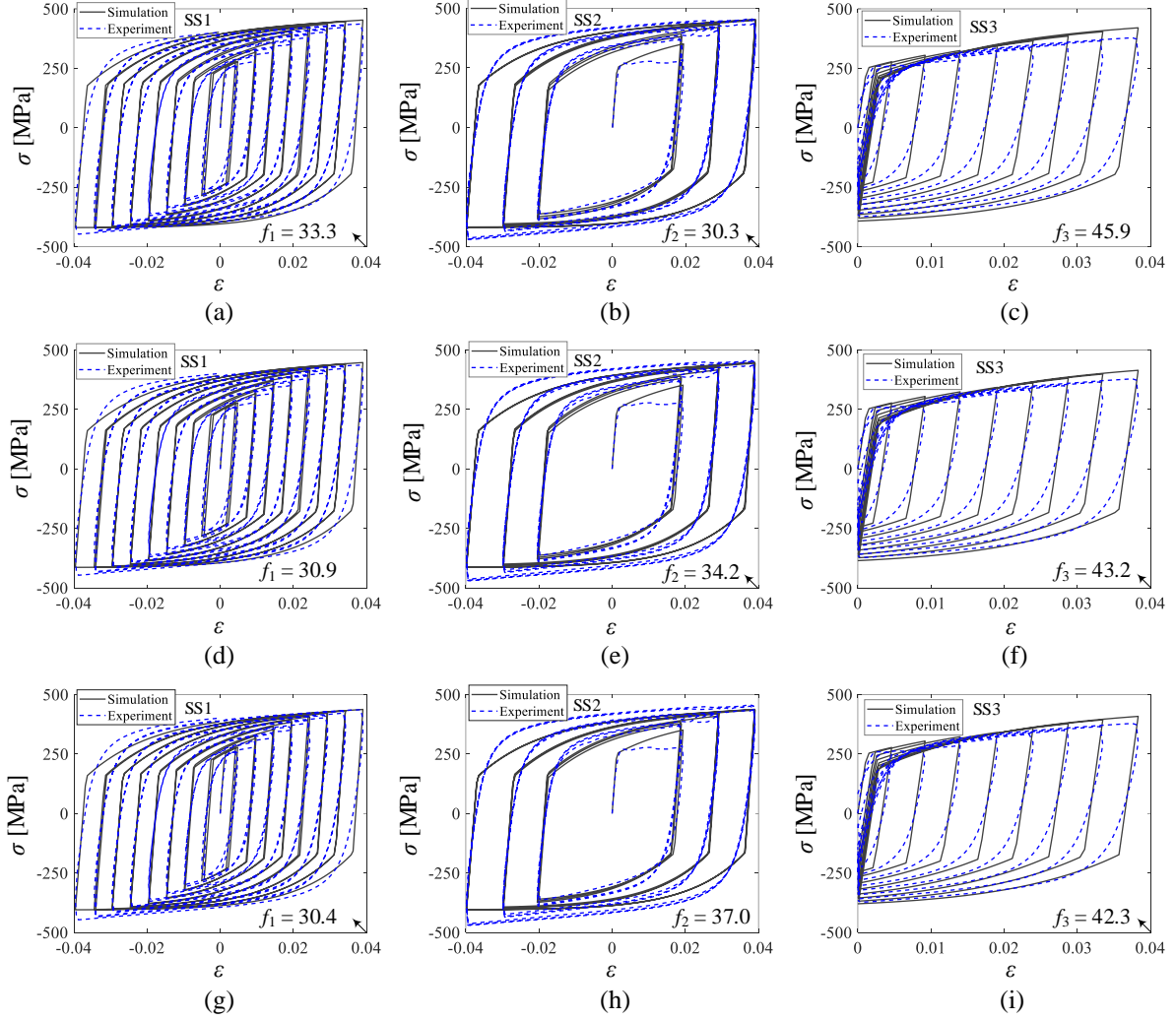


Fig. 8: Comparison of test data and model predictions for cyclic tests of the specimen with the best compromise solutions of parameters identified from different groups of experimental datasets. (a), (b), (c) Parameters from group 1; (d), (e), (f) Parameters from group 2; (g), (h), (i) Parameters from group 3.

Table 6: Dataset-specific indexes for different sets of identification results evaluated using the experimental results from tests SN1, SNR2, and SSR1 of the specimen [MPa].

Set of results	ψ_4	ψ_5	ψ_6	ξ
Multi-objective (1)	8.359	7.567	1.087	5.671
Multi-objective (2)	9.318	8.441	1.440	6.400
Single-objective	19.911	28.040	2.050	16.667
Weighted-sum	11.319	10.202	0.914	7.478

identification. Although the yield plateau observed in test SS2 cannot be captured because of the nature of the nonlinear combined isotropic/kinematic hardening model, the identified parameters can reproduce the $\sigma - \epsilon$

curves for the loading histories not used for identification with good accuracy. To strengthen this conclusion, we further use each set of parameters in Table 4 to predict the $\sigma - \epsilon$ curves from other three loading histories SN1, SNR2, and SSR1 that have not been seen in the identification, but were used by Yamada and Jiao (2016) in other cyclic tests. The ξ index in Eq. (21) is also evaluated for each set of identification results using the error function values of tests SN1, SNR2, and SSR1, namely, f_4 , f_5 , and f_6 , respectively. In this case, ξ represents the dispersion of predictions by the associated parameter sets because SN1, SNR2, and SSR1 are not used for identification, and f_j^{\min} and f_j^{\max} in Eq. (21) both indicate the prediction performance of the associated parameter sets. Fig. 9 shows the ability

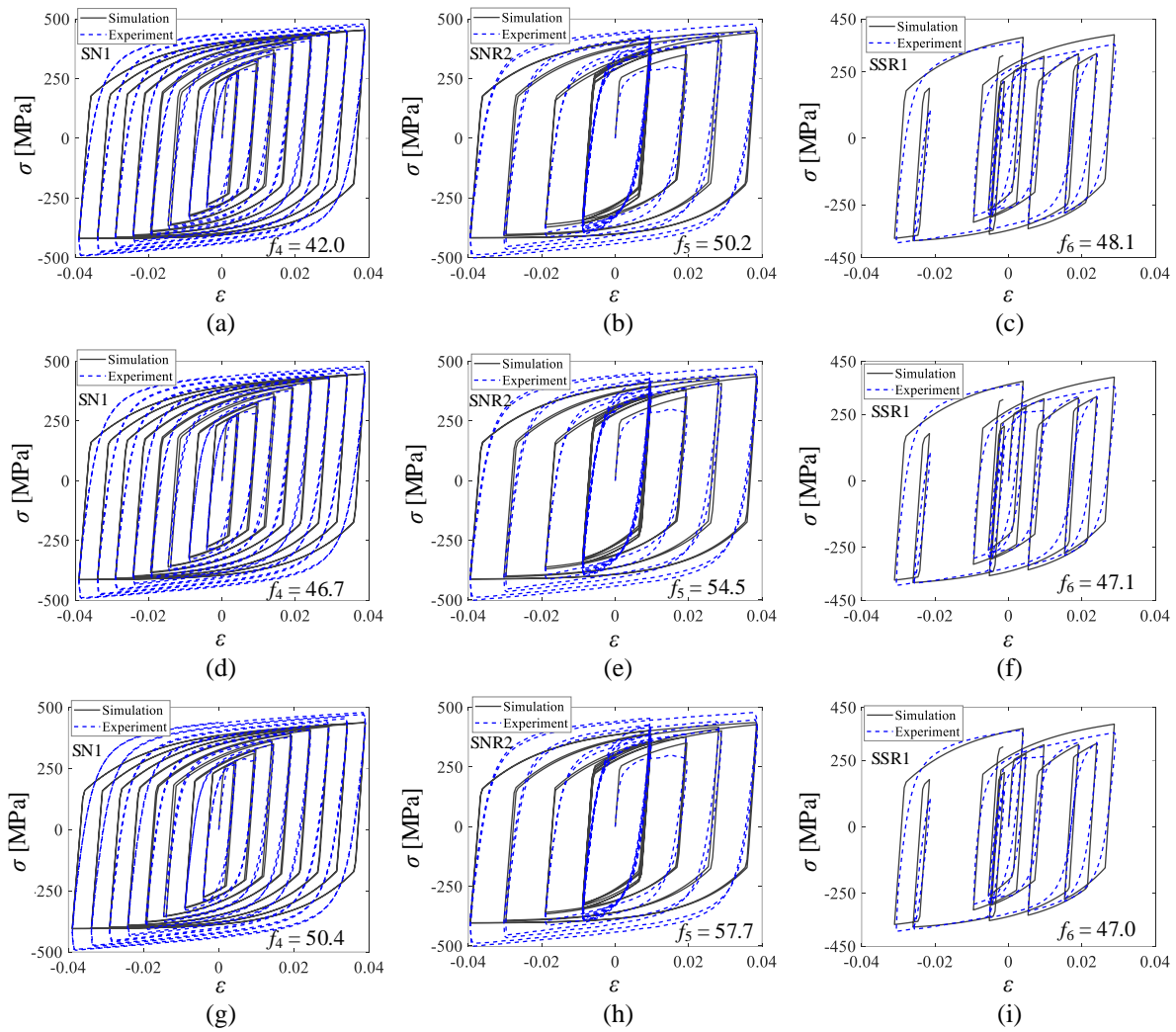


Fig. 9: Comparison of test data and model predictions for other cyclic tests of the specimen, which are not used for identification, with the best compromise solutions of parameters identified from different groups of experimental datasets. (a), (b), (c) Parameters from group 1; (d), (e), (f) Parameters from group 2; (g), (h), (i) Parameters from group 3.

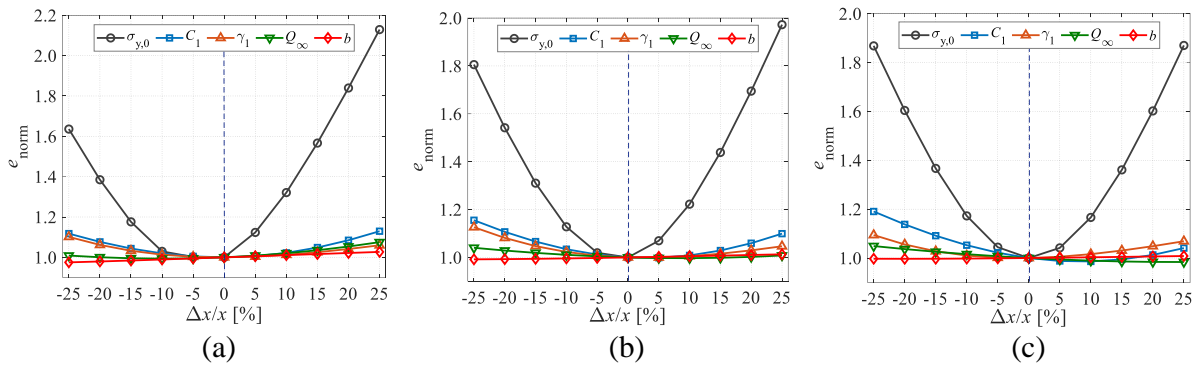


Fig. 10: Average sensitivity results over different groups of experimental datasets from cyclic tests of the specimen. (a) Parameters from group 1; (b) Parameters from group 2; (c) Parameters from group 3.

of the best-compromise solutions to predict the $\sigma - \epsilon$ curves from SN1, SNR2, and SSR1. Table 6 provides the ξ index values evaluated for each set of identification results listed in Table 4 using f_4 , f_5 , and f_6 . It is confirmed that ξ values for the two sets of identification results from the multi-objective formulation are smaller than those corresponding to the single-objective and weighted-sum formulations, indicating the reliability of predictions by the solutions to the multi-objective inverse problem for the specimen.

To further rank the importance of the identified material parameters, we assess the sensitivity of the error functions to the variation of each parameter, indicated by the ratio $\Delta x/x$, in the neighborhood of its best compromise value (in the parameter space) as shown in Fig. 10 while keeping other parameters constant. The sensitivity of each error function is represented by e_{norm} that is defined as the ratio of the error function of interest to that associated with the best compromise solution. Thus, the sensitivity result at a particular value of $\Delta x/x$, as shown in Fig. 10, is the average of three e_{norm} values corresponding to the three error functions f_1 , f_2 , and f_3 . As observed, the error functions are most and least sensitive to the variations of $\sigma_{y,0}$ and b , respectively.

5.2 Parameters for a bi-material cantilever

We use MOBO to identify the parameters for a steel cantilever tested under three different static cyclic loading histories RH1, RH2, and RH3 as shown in Fig. 11. The cantilever is a built-up wide-flange beam H-244 \times 175 \times 7 \times 11 in Japanese specification. The web and flange have the same Young's modulus, but different plastic material parameters. Thus, the cantilever is a structural component of two different materials. During the tests conducted by Yamada and Jiao (2016), the left end of the cantilever was fixed, while forced vertical displacement was applied at the right end. The deflection angle θ of the cantilever was defined as the ratio of the vertical tip displacement Δ mm to the beam length $L = 800$ mm, i.e., $\theta = \Delta/L$.

The test results for the three loading histories consist of three experimental datasets of the bending moment M at the cantilever support and the associated deflection angle θ . To investigate how the experimental datasets used for identification affect the resulting parameters, the three experimental datasets are classified into three different groups indexed as 1, 2, 3, which correspond to RH1 & RH2, RH2 & RH3, and RH3 & RH1, respectively. To examine the robustness of MOBO, each group generates ten different training datasets at the beginning of MOBO. Each of these training datasets

has 100 random samples of material parameters and the corresponding error function values.

We model the cantilever using Abaqus (Dassault Systèmes, 2017) for evaluation of the error function values associated with each parameter sample. A fine mesh consisting of 4960 nodes and 3510 linear hexahedral elements of type C3D8 is generated, as shown in Fig. 11, for reducing the sensitivity of simulation results to the FE mesh density. The maximum increment size for each loading history is set as 0.01 s.

Table 7: Material parameter intervals for the cantilever.

	Parameter	Lower bound	Upper bound
Web	E [GPa]	175.05	–
	$\sigma_{y,0}$ [MPa]	300	340
	Q_∞ [MPa]	10	100
	b	5	25
	C_1 [MPa]	2000	8000
	γ_1	10	100
Flange	E [GPa]	175.05	–
	$\sigma_{y,0}$ [MPa]	270	290
	Q_∞ [MPa]	10	100
	b	5	25
	C_1 [MPa]	2000	8000
	γ_1	10	100

Table 8: Optimized HVs associated with ten MOBO attempts for different groups of experimental datasets from cyclic tests of the cantilever [$\times 10^2$ (kNm) 2].

Attempt	Group 1	Group 2	Group 3
1	15.444	14.547	14.509
2	15.570	14.403	14.630
3	15.514	14.583	14.772
4	15.613	14.608	14.928
5	15.566	14.575	14.886
6	15.513	14.673	14.687
7	15.619	14.652	14.737
8	15.399	14.490	14.375
9	15.411	14.596	14.378
10	15.581	14.478	14.732

We carry out MOBO for the ten different training datasets of each group, which, therefore, provides ten Pareto fronts of material parameters. The number of MOBO iterations is limited at 50. Thus, the maximum number of simulations required for each MOBO attempt is 300 (i.e., 200 for generation of the initial training dataset and maximum 100 for MOBO iterations). The reference point and the parameter β are set as $\mathbf{f}_R = [50, 50]$ kNm and 0.01, respectively. Problem (14) in each MOBO iteration is solved using GA,

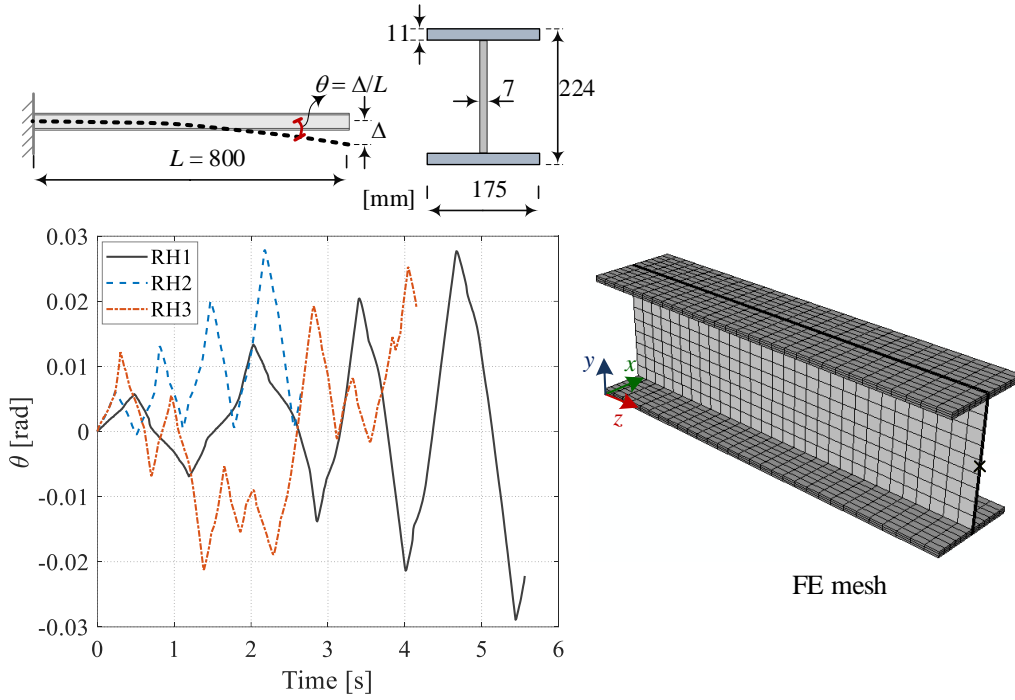


Fig. 11: Bi-material cantilever, its FE mesh, and three loading histories for cyclic tests (Do and Ohsaki, 2022a; Yamada and Jiao, 2016).

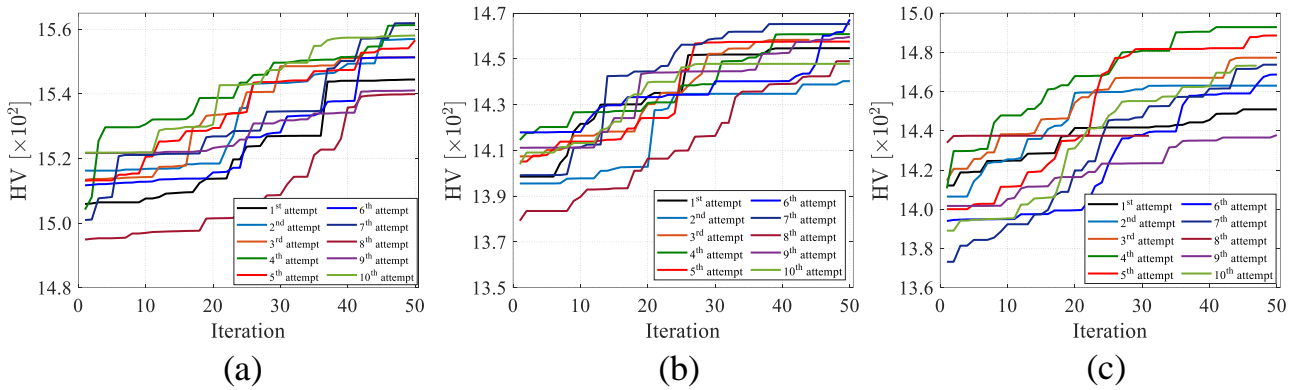


Fig. 12: Histories of HVs for different groups of experimental datasets from cyclic tests of the cantilever. (a) From group 1; (b) From group 2; (c) From group 3.

whose parameters are the same as those for the GA in Section 5.1. Poisson's ratio and Young's modulus for the web and flange are kept constant at 0.3 and $E = 175.05$ GPa (Yamada and Jiao, 2016), respectively. Therefore, a total of ten material parameters are identified for the cantilever (i.e., five for the web and five for the flange). The interval associated with each parameter, as provided in Table 7, is taken from Do and Ohsaki (2022a). To enable a favorable comparison of the identified parameters, we also perform NSGA-II ten times for finding Pareto fronts for each group. Each NSGA-II is characterized by a population of 30 individuals and

five generations, thereby requiring a total of 300 simulations, which is the same as the maximum number of simulations required for MOBO.

Fig. 12 shows the histories of HV from the ten MOBO attempts of each group. Although the MOBO attempts starting at different initial training datasets cannot arrive at a unique value of HV after 50 iterations, they considerably improve the solution quality. Since the HVs from most of the MOBO attempts tend to improve in the very last iterations, we may expect that the solutions from each group can be improved if the number of MOBO iterations is increased. The optimized HVs cor-

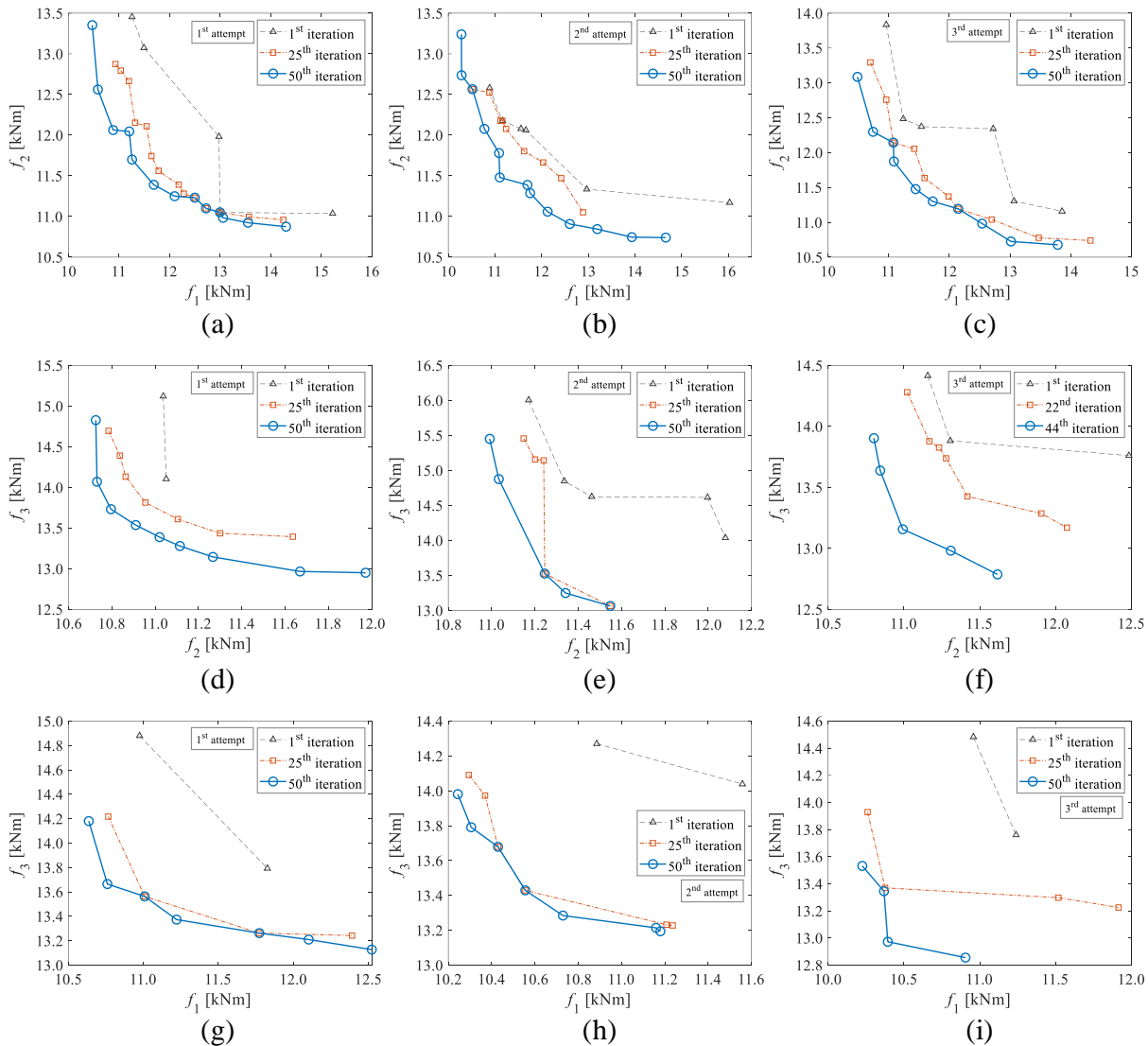


Fig. 13: Evolution of approximate Pareto-optimal solutions during the first three MOBO attempts for different groups of experimental datasets from cyclic tests of the cantilever. (a), (b), (c) From group 1; (d), (e), (f) From group 2; (g), (h), (i) From group 3.

responding to the ten MOBO attempts of each group are listed in Table 8. Fig. 13 shows the evolution of approximate Pareto-optimal solutions during the first three MOBO attempts of each group. As is clear, the solutions in the last iteration of MOBO are much better than those in the very first iteration. Fig. 14 compares the Pareto fronts from ten MOBO attempts and ten NSGA-II attempts of each group. The shapes of the Pareto fronts by the ten MOBO attempts of the first group are similar (see Fig. 14(a)), but those of the other two groups are not (see Figs. 14(c) and (d)). The solutions by the MOBO attempts in each group outperform those by the NSGA-II attempts even though the

number of costly simulations required for MOBO does not exceed that required for NSGA-II.

Table 9 lists the best (1) and second-best (2) compromise solutions on the Pareto front having the highest HV among the ten Pareto fronts found from each group. The error function values corresponding to RH1, RH2, and RH3, denoted as f_1 , f_2 , and f_3 , respectively, are also provided. Values of $\sigma_{y,0}$, Q_∞ , and b for the flange among those from different groups are similar, while those of C_1 and γ_1 are group-dependent. A change in the dataset (i.e., group) itself can lead to a major difference in the identified parameters for the web although these parameters are possible to produce the simulated

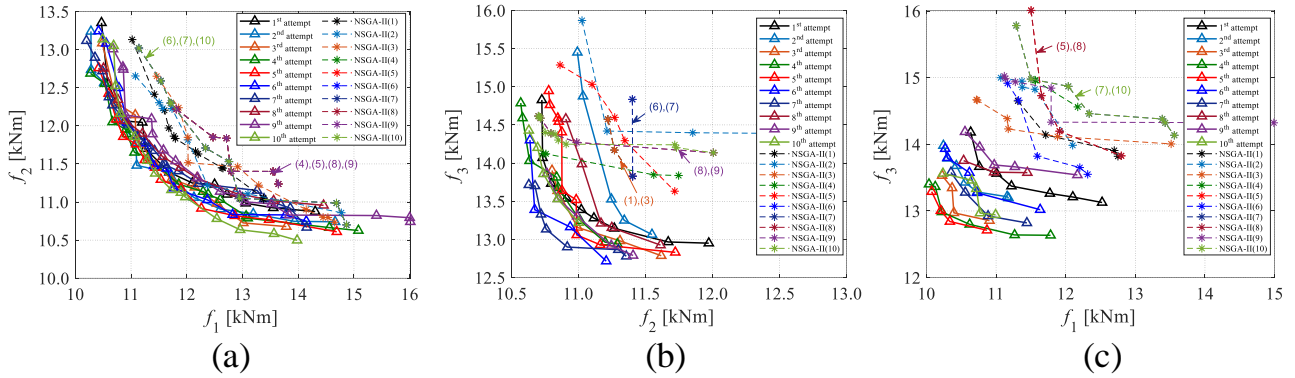


Fig. 14: Comparison of solutions by ten MOBO attempts and by ten NSGA-II attempts for different groups of experimental datasets from cyclic tests of the cantilever. (a) From group 1; (b) From group 2; (c) From group 3.

responses consistent with the corresponding experimental measures. This is due to bending dominates in the tests, and the shear in web is not a major factor.

Fig. 15 compares the predicted and measured $M - \theta$ curve from each loading history with use of the best compromise parameters identified from each group for prediction. As observed, the parameters well reproduce the $M - \theta$ curves corresponding to the loading history that is not used for identification. Although there exists the bias toward the loading history used for identification, its effect on the prediction performance of identified parameters is not significant as the corresponding minimized error function value is slightly smaller than that predicted from the parameters identified from the other loading histories (see along each column of Fig. 15). It would be more interesting if the identified parameters can be used to predict the uniaxial cyclic behavior of the flange and the cyclic bending behavior of the web. However, the associated material cyclic tests are not available.

With RH1, RH2, and RH3, other six single-objective inverse problems are formulated for the cantilever using the single-objective and weighted-sum formulations to investigate the dataset-bias levels of different sets of identification results from different formulations of the inverse problem of the cantilever. Three problems associated with the single-objective formulation, namely, SIG 1, SIG 2, SIG 3 are formulated from RH1, RH2, and RH3, respectively. Those associated with the weighted-sum formulation, namely, SUM 1, SUM 2, SUM 3 are formulated from RH1 & RH2, RH2 & RH3, and RH3 & RH1, respectively. These problems have been successfully solved using the standard BO and the solution to each problem is reported in Table 10 (Do and Ohsaki, 2022a). From the results in Tables 9 and 10, ξ index in Eq. (21) is evaluated for the parameter sets of the best and second-best compromise solutions by the

multi-objective formulation and for those by the single-objective and weighted-sum formulations. Results in Table 11 indicate that ξ values for the best and second-best compromise sets of identification results from the multi-objective formulation are better than those from the single-objective and weighted-sum formulations. The single-objective formulation again shows the largest value of the data-specific bias level.

Fig. 16 shows the sensitivity results for each best compromise parameters identified from the three experimental dataset groups of the cantilever. The high-sensitivity parameters include $\sigma_{y,0}$ of the flange and web, and C_1 of the flange, in which $\sigma_{y,0}$ of the flange has the greatest influence on the sensitivity of the error functions. Other parameters can be classified as low-sensitivity parameters.

6 Conclusions

The dataset-specific bias may lead the elastoplastic parameters for the cyclic constitutive law identified from a single loading history to inaccurate predictions of structural responses under other loading histories. If the cyclic behavior of the material (or structural component) subjected to different loading histories is measured experimentally, a multi-objective inverse problem to reduce the dataset-specific bias can be formulated for identifying the material parameters. Such an inverse problem is also desirable because it offers an approximate Pareto front of parameters that allows designers to flexibly select the material parameters for their designs while the parameter identification is performed only once. This work has proposed an efficient proximal-exploration MOBO approach to solving the aforementioned inverse problem. MOBO generates a small number of material parameter sets and sorts an approximate

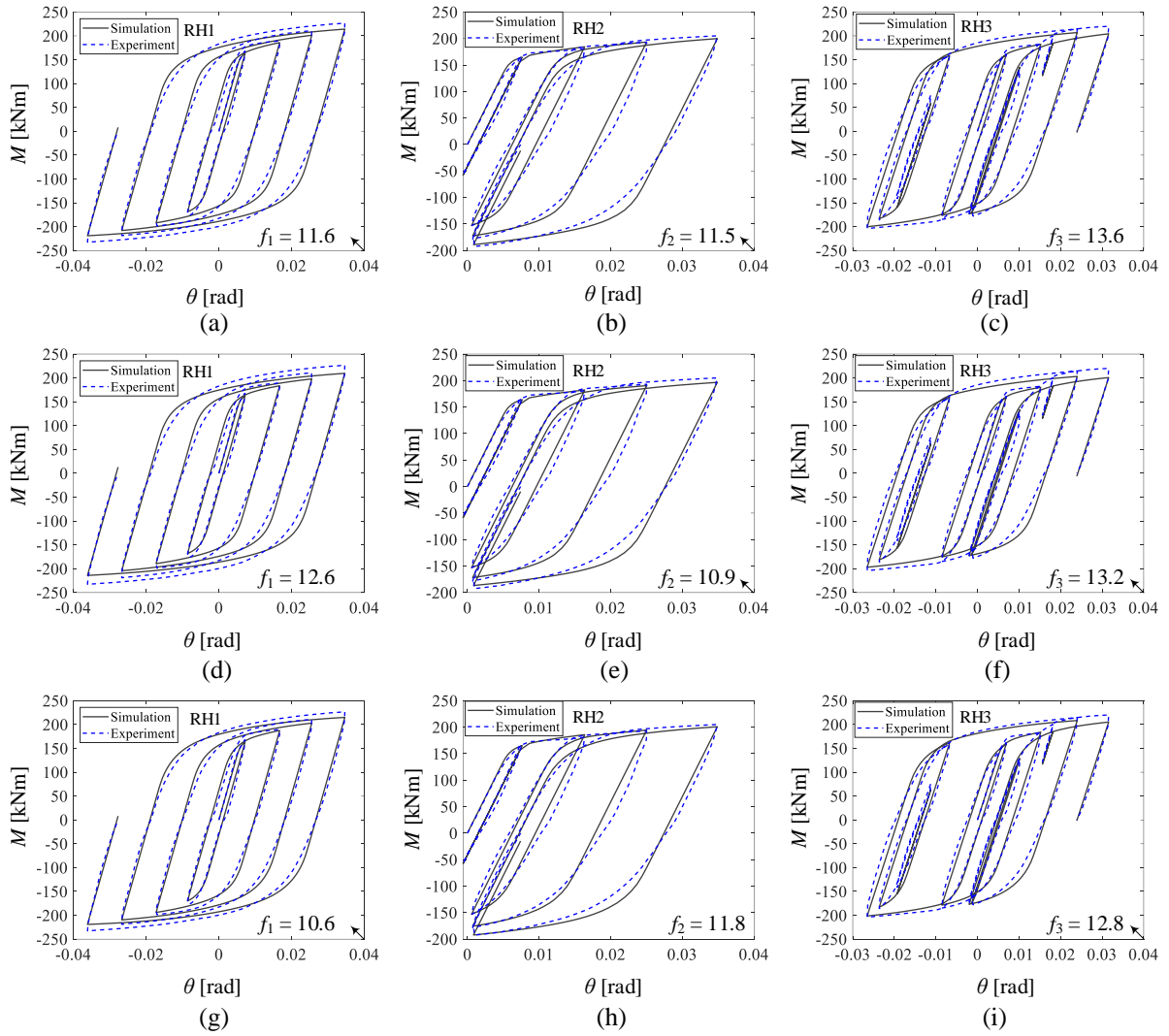


Fig. 15: Comparison of test data and model predictions for cyclic tests of the cantilever with the best compromise solutions of parameters identified from different groups of experimental datasets. (a), (b), (c) Parameters from group 1; (d), (e), (f) Parameters from group 2; (g), (h), (i) Parameters from group 3.

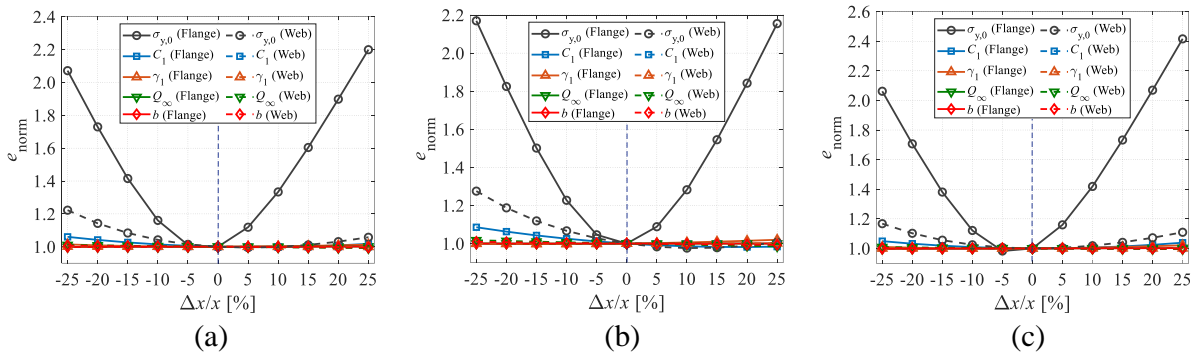


Fig. 16: Average sensitivity results over different groups of experimental datasets from cyclic tests of the cantilever. (a) Parameters from group 1; (b) Parameters from group 2; (c) Parameters from group 3.

Table 9: Comparison of the best and second-best compromise solutions of identified material parameters and error functions obtained from MOBO for different groups of experimental datasets of the cantilever.

	Parameter	Group					
		1 (1)	2 (1)	3 (1)	1 (2)	2 (2)	3 (2)
Web	$\sigma_{y,0}$ [MPa]	305.738	325.737	338.125	311.831	326.628	334.007
	Q_∞ [MPa]	99.938	76.621	99.813	82.085	86.073	99.751
	b	15.077	23.777	24.937	19.234	24.933	24.997
	C_1 [MPa]	6013.083	3405.444	5691.577	5477.573	5946.957	2665.344
	γ_1	66.381	99.536	99.964	35.927	99.909	99.940
Flange	$\sigma_{y,0}$ [MPa]	273.851	270.577	270.007	273.761	271.079	270.233
	Q_∞ [MPa]	12.268	10.315	14.499	10.191	10.517	10.025
	b	6.426	8.090	5.001	6.521	5.783	5.220
	C_1 [MPa]	7502.126	6315.732	7316.046	7410.770	4904.880	7030.846
	γ_1	73.482	58.928	76.793	73.137	44.959	79.902
Error	f_1 [kNm]	11.607	12.571	10.621	11.596	13.360	11.783
	f_2 [kNm]	11.489	10.937	11.846	11.517	10.672	11.458
	f_3 [kNm]	13.630	13.163	12.799	13.660	13.390	12.635

Table 10: Material parameters and error functions obtained from solving single-objective inverse problems using the standard BO for different groups of experimental datasets of the cantilever (Do and Ohsaki, 2022a).

	Parameter	Group					
		SIG 1	SIG 2	SIG 3	SUM 1	SUM 2	SUM 3
Web	$\sigma_{y,0}$ [MPa]	339.957	300.049	339.924	336.672	330.990	339.880
	Q_∞ [MPa]	99.890	99.827	99.923	99.874	99.972	99.974
	b	24.946	24.910	24.952	24.761	24.809	24.869
	C_1 [MPa]	7160.521	7968.280	3596.024	7766.642	7999.973	7682.000
	γ_1	99.622	10.178	99.967	99.999	69.775	99.577
Flange	$\sigma_{y,0}$ [MPa]	271.262	270.004	270.047	270.008	270.001	270.061
	Q_∞ [MPa]	10.065	10.135	10.000	10.140	10.107	10.001
	b	5.008	5.120	5.047	5.534	5.092	5.041
	C_1 [MPa]	7999.840	5170.983	6636.794	6537.440	5140.712	7998.996
	γ_1	66.632	62.092	71.565	60.903	69.258	84.763
Error	f_1 [kNm]	10.083	14.166	11.469	10.781	12.760	10.107
	f_2 [kNm]	12.836	10.422	11.377	11.491	10.794	12.380
	f_3 [kNm]	13.601	14.060	12.590	12.959	12.881	12.961

Table 11: Dataset-specific indexes for different sets of identification results evaluated using the experimental results from three tests of the cantilever [kNm].

Set of results	ψ_1	ψ_2	ψ_3	ξ
Multi-objective (1)	1.950	0.909	0.831	1.230
Multi-objective (2)	1.765	0.844	1.025	1.211
Single-objective	4.083	2.414	1.470	2.656
Weighted-sum	2.653	1.586	0.080	1.440

Pareto front from them. The approximate Pareto front is sequentially improved by maximizing an acquisition function formulated for selecting a new, promising vector of parameters in the next iteration of MOBO without calling any simulation, thereby considerably reducing the computational cost.

Using a limited number of simulation calls, MOBO has successfully identified a good approximate Pareto front of elastoplastic parameters for the nonlinear combined isotropic/kinematic hardening model for a steel specimen and a cantilever tested under different static cyclic loadings. The identification results show that the best compromise solution of identified parameters well captures the cyclic behavior of the steel under different loading conditions. Nevertheless, other solutions on the Pareto front may be used for structural response predictions according to the characteristic of design cyclic loadings. The identification results for the cantilever also suggest a possibility of identifying material parameters from cyclic tests of a structural component with two different materials. This is notable because cyclic material tests are difficult and usually not carried out before structural tests. Moreover, since some param-

eters of the two steel materials in the second identification example may be insensitive, a regularization penalty can be applied to reduce the variations of low-sensitivity parameters.

A data-specific index ξ has been proposed for assessing the data-specific bias levels for different sets of identification results obtained from different inverse problem formulations. Based on ξ , we have shown in two identification examples that the best and second-best compromise solutions to the multi-objective inverse problem can reduce the dataset-specific bias, while the solution to the single-objective formulation shows an enormous bias level. The index ξ can also be used for assessing the reliability of predictions by the available parameters on a set of experimental results not used for identification.

The proposed MOBO demonstrates its good performance in solving a simple bi-objective minimization problem. As also confirmed in the identification examples, MOBO outperforms NSGA-II in terms of solution quality when expending the same number of simulation calls. Thus, future works may apply or extend the algorithm to solving multi-objective structural optimization problems that have costly objective and/or constraint functions. Moreover, since the proposed MOBO has only been tested against problems with two (i.e., test problem), five (i.e., specimen problem), and ten (i.e., cantilever problem) dimensions while the BO approach is suitable for problems of less than 20 dimensions (Frazier, 2018), it is desirable to extend the application of MOBO to solving high-dimensional inverse problems, for example, finding the parameters for a structure. Another extension of MOBO to optimization problems with qualitative or mixed-integer design variables, which are often encountered in structural design, may also be an interesting topic of future research.

The multi-objective inverse problems in Section 5 are formulated based on only three sets of experimental results. Therefore, it is desirable to scale up the application of the multi-objective formulation to the case where a dozen of sets of experimental results are available. Either of the following two strategies may be applicable. First, the experimental sets can be split into disjoint clusters based on the similarity or the correlation between the test results. In this way, improving the objective value of a set may not worsen the objective values of other sets in the same cluster and therefore, each cluster can be represented by a single objective function, which is formulated from a representative set or from individual objectives of the sets in that cluster using the weighted-sum approach. Second, if it is not clear to determine the similarity or correlation between the experimental sets, the multi-objective inverse prob-

lem can also be formulated for every combination of three sets, and the remaining sets are used for validation. Three sets for each combination are recommended because they allow us to visualize how the solutions are distributed in the objective function space. Then, the ξ index values for the solutions to each problem can be evaluated using the associated validation sets. As a result, different sets of ξ index values can be found based on the validation sets for rational decision-making.

Acknowledgements This study was supported by the JICA AUN/SEED-Net project and by JSPS KAKENHI Grant Number JP19H02286. We would like to thank Prof. Satoshi Yamada at The University of Tokyo for providing all experimental results used in this work. We also would like to thank the anonymous reviewers for their valuable comments and suggestions that have significantly contributed to the improvement of our paper.

Declarations

Conflict of interest

The authors declare that they have no conflict of interest.

Replication of results

Main source codes used for solving the test problem in Section 4 and the identification problem in Section 5.1, and the loading histories in Section 5.2 are available online at <https://github.com/BachDo17/InverseMOBO>. An Abaqus input file for use of licensed users to solve the problem in Section 5.2 is available from the corresponding author by request.

Appendix: Gaussian process (GP)

Consider the training dataset $\mathcal{D} = \{\mathbf{X}, \mathbf{f}\} = \{\mathbf{x}_k, f_k\}_{k=1}^N$, where $\mathbf{x}_k \in \mathbb{R}^n$ are n -dimensional vectors of the material parameters and $f_k \in \mathbb{R}$ the corresponding error function values. We establish the relationship between \mathbf{x} and f using the mapping $f = \hat{f}(\mathbf{x}) : \mathbb{R}^n \rightarrow \mathbb{R}$, where $\hat{f}(\mathbf{x})$ is a Gaussian conditioned on \mathcal{D} .

A GP assumes that any finite subset of an infinite set of the error function values has a joint Gaussian distribution (Rasmussen and Williams, 2006). Thus, for the set of N parameter vectors $\{\mathbf{x}_1, \dots, \mathbf{x}_N\}$, the corresponding error function values $\{f_1, \dots, f_N\}$ are distributed according to

$$\begin{bmatrix} f_1 \\ \vdots \\ f_N \end{bmatrix} \sim \mathcal{N}_N \left(\begin{bmatrix} m(\mathbf{x}_1) \\ \vdots \\ m(\mathbf{x}_N) \end{bmatrix}, \begin{bmatrix} k(\mathbf{x}_1, \mathbf{x}_1) & \cdots & k(\mathbf{x}_1, \mathbf{x}_N) \\ \vdots & \ddots & \vdots \\ k(\mathbf{x}_N, \mathbf{x}_1) & \cdots & k(\mathbf{x}_N, \mathbf{x}_N) \end{bmatrix} \right) \quad (\text{A.1})$$

where \mathcal{N}_N denotes an N -variate Gaussian; and $m(\mathbf{x}) = \mathbb{E}[\hat{f}(\mathbf{x})]$ and $k(\mathbf{x}, \mathbf{x}')$ the mean and covariance kernel functions, respectively. The mean function in this study is set as $m(\mathbf{x}) = 0$ because the covariance kernel function is flexible enough to handle the role of $m(\mathbf{x})$ (Rasmussen and Williams, 2006). The covariance kernel function is defined for any pair of the parameter vectors \mathbf{x} and \mathbf{x}' to measure the similarity between two corresponding error function values $f = \hat{f}(\mathbf{x})$ and $f = \hat{f}(\mathbf{x}')$, such that

$$k(\mathbf{x}, \mathbf{x}') = \mathbb{E}[(\hat{f}(\mathbf{x}) - m(\mathbf{x}))(\hat{f}(\mathbf{x}') - m(\mathbf{x}'))] \quad (\text{A.2})$$

Here we use Gaussian kernel as

$$k(\mathbf{x}, \mathbf{x}') = \exp\left(-\frac{(\mathbf{x} - \mathbf{x}')^T(\mathbf{x} - \mathbf{x}')}{2l^2}\right) \quad (\text{A.3})$$

where l denotes the characteristic length-scale parameter that is determined by using the maximum likelihood estimation of \mathcal{D} (Rasmussen and Williams, 2006).

Once l has been determined based on \mathcal{D} , we wish to use the information in Eq. (A.1) for predicting the error function value f^* at a new parameter vector \mathbf{x}^* , i.e., $f^*|\mathbf{f} = \hat{f}(\mathbf{x}^*)$. As the GP nature, the joint PDF of f^* and \mathbf{f} is also a Gaussian. Let $\mathbf{m}(\mathbf{X}) = [m(\mathbf{x}_1), \dots, m(\mathbf{x}_N)]^T$, we have

$$\begin{bmatrix} f^* \\ \mathbf{f} \end{bmatrix} \sim \mathcal{N}_{N+1}\left(\begin{bmatrix} m(\mathbf{x}^*) \\ \mathbf{m}(\mathbf{X}) \end{bmatrix}, \begin{bmatrix} k(\mathbf{x}^*, \mathbf{x}^*) & \mathbf{K}(\mathbf{x}^*, \mathbf{X}) \\ \mathbf{K}(\mathbf{x}^*, \mathbf{X})^T & \mathbf{K}(\mathbf{X}, \mathbf{X}) \end{bmatrix}\right) \quad (\text{A.4})$$

where

$$\mathbf{K}(\mathbf{x}^*, \mathbf{X}) = [k(\mathbf{x}^*, \mathbf{x}_1), \dots, k(\mathbf{x}^*, \mathbf{x}_N)] \quad (\text{A.5})$$

$$\mathbf{K}(\mathbf{X}, \mathbf{X}) = \begin{bmatrix} k(\mathbf{x}_1, \mathbf{x}_1) & \cdots & k(\mathbf{x}_1, \mathbf{x}_N) \\ \vdots & \ddots & \vdots \\ k(\mathbf{x}_N, \mathbf{x}_1) & \cdots & k(\mathbf{x}_N, \mathbf{x}_N) \end{bmatrix} \quad (\text{A.6})$$

The conditional Gaussian variable $f^*|\mathbf{f} = \hat{f}(\mathbf{x}^*)$ can be derived from Eq. (A.4) using the standard conditioning rule (Rasmussen and Williams, 2006), such that

$$f^*|\mathbf{f} \sim \mathcal{N}(\mu_{f^*}(\mathbf{x}^*), \tau_{f^*}^2(\mathbf{x}^*)) \quad (\text{A.7})$$

where

$$\mu_{f^*}(\mathbf{x}^*) = m(\mathbf{x}^*) + \mathbf{K}(\mathbf{x}^*, \mathbf{X})\mathbf{K}(\mathbf{X}, \mathbf{X})^{-1}(\mathbf{f} - \mathbf{m}(\mathbf{X})) \quad (\text{A.8})$$

$$\tau_{f^*}^2(\mathbf{x}^*) = k(\mathbf{x}^*, \mathbf{x}^*) - \mathbf{K}(\mathbf{x}^*, \mathbf{X})\mathbf{K}(\mathbf{X}, \mathbf{X})^{-1}\mathbf{K}(\mathbf{x}^*, \mathbf{X})^T \quad (\text{A.9})$$

References

Abido MA (2003) A novel multiobjective evolutionary algorithm for environmental/economic power dispatch. *Electric Power Systems Research* 65(1):71–81, doi:[10.1016/S0378-7796\(02\)00221-3](https://doi.org/10.1016/S0378-7796(02)00221-3)

Armstrong PJ, Frederick CO (1966) A mathematical representation of the multiaxial Bauschinger effect. Report RD/B/N731, Berkeley, UK

Arridge S, Maass P, Öktem O, Schönlieb CB (2019) Solving inverse problems using data-driven models. *Acta Numerica* 28:1–174, doi:[10.1017/S0962492919000059](https://doi.org/10.1017/S0962492919000059)

Beck JL, Katafygiotis LS (1998) Updating models and their uncertainties. I: Bayesian statistical framework. *Journal of Engineering Mechanics* 124(4):455–461, doi:[10.1061/\(ASCE\)0733-9399\(1998\)124:4\(455\)](https://doi.org/10.1061/(ASCE)0733-9399(1998)124:4(455))

Carreño R, Lotfizadeh K H, Conte J P, Restrepo J I (2020) Material model parameters for the Giuffrè-Menegotto-Pinto uniaxial steel stress-strain model. *Journal of Structural Engineering* 146(2):04019205, doi:[10.1061/\(ASCE\)ST.1943-541X.0002505](https://doi.org/10.1061/(ASCE)ST.1943-541X.0002505)

de Carvalho R, Valente RAF, Andrade-Campos A (2011) Optimization strategies for non-linear material parameters identification in metal forming problems. *Computers & Structures* 89(1):246–255, doi:[10.1016/j.compstruc.2010.10.002](https://doi.org/10.1016/j.compstruc.2010.10.002)

Chaboche JL (2008) A review of some plasticity and viscoplasticity constitutive theories. *International Journal of Plasticity* 24(10):1642–1693, doi:[10.1016/j.ijplas.2008.03.009](https://doi.org/10.1016/j.ijplas.2008.03.009)

Chaboche JL, Rousselier G (1983) On the plastic and viscoplastic constitutive equations—Part I: Rules developed with internal variable concept. *Journal of Pressure Vessel Technology* 105(2):153–158, doi:[10.1115/1.3264257](https://doi.org/10.1115/1.3264257)

Chaparro BM, Thuillier S, Menezes LF, Manach PY, Fernandes JV (2008) Material parameters identification: Gradient-based, genetic and hybrid optimization algorithms. *Computational Materials Science* 44(2):339–346, doi:[10.1016/j.commatsci.2008.03.028](https://doi.org/10.1016/j.commatsci.2008.03.028)

Couckuyt I, Deschrijver D, Dhaene T (2014) Fast calculation of multiobjective probability of improvement and expected improvement criteria for Pareto optimization. *Journal of Global Optimization* 60(3):575–594, doi:[10.1007/s10898-013-0118-2](https://doi.org/10.1007/s10898-013-0118-2)

Dassault Systèmes (2017) Abaqus User’s Manual Version 2017

Daulton S, Eriksson D, Balandat M, Bakshy E (2021) Multi-objective Bayesian optimization over high-dimensional search spaces. arXiv preprint [arXiv:2109.10964](https://arxiv.org/abs/2109.10964)

Deb K, Pratap A, Agarwal S, Meyarivan T (2002) A fast and elitist multiobjective genetic algorithm: NSGA-II. *IEEE transactions on evolutionary computation* 6(2):182–197, doi:[10.1109/4235.996017](https://doi.org/10.1109/4235.996017)

Do B, Ohsaki M (2022a) Bayesian optimization for inverse identification of cyclic constitutive law of structural steels from cyclic structural tests. *Structures* 38:1079–1097, doi:[10.1016/j.istruc.2022.02.054](https://doi.org/10.1016/j.istruc.2022.02.054)

Do B, Ohsaki M (2022b) Sequential sampling approach to energy-based multi-objective design optimization of steel frames with correlated random parameters. *Earthquake Engineering and Structural Dynamics* 51(3):588–611, doi:[10.1002/eqe.3581](https://doi.org/10.1002/eqe.3581)

Do B, Ohsaki M, Yamakawa M (2021) Bayesian optimization for robust design of steel frames with joint and individual probabilistic constraints. *Engineering Structures* 245:112859, doi:[10.1016/j.engstruct.2021.112859](https://doi.org/10.1016/j.engstruct.2021.112859)

Emmerich MTM, Giannakoglou KC, Naujoks B (2006) Single- and multiobjective evolutionary optimization assisted by Gaussian random field metamodells. *IEEE Transactions on Evolutionary Computation* 10(4):421–439, doi:[10.1109/TEVC.2005.859463](https://doi.org/10.1109/TEVC.2005.859463)

Feliot P, Bect J, Vazquez E (2017) A Bayesian approach to constrained single- and multi-objective optimization. *Journal of Global Optimization* 67(1):97–133, doi:[10.1007/s10898-016-0427-3](https://doi.org/10.1007/s10898-016-0427-3)

Fonseca CM, Paquete L, Lopez-Ibanez M (2006) An improved dimension-sweep algorithm for the hypervolume indicator. In: 2006 IEEE International Con-

- ference on Evolutionary Computation, pp 1157–1163, doi:[10.1109/CEC.2006.1688440](https://doi.org/10.1109/CEC.2006.1688440)
- Frazier PI (2018) A tutorial on Bayesian optimization. arXiv preprint [arXiv:1807.02811](https://arxiv.org/abs/1807.02811)
- Hartloper AR, de Castro e Sousa Albano, Lignos DG (2021) Constitutive modeling of structural steels: nonlinear isotropic/kinematic hardening material model and its calibration. *Journal of Structural Engineering* 147(4):04021031, doi:[10.1061/\(ASCE\)ST.1943-541X.0002964](https://doi.org/10.1061/(ASCE)ST.1943-541X.0002964)
- Jekel CF, Venter G, Venter MP, Stander N, Haftka RT (2019) Similarity measures for identifying material parameters from hysteresis loops using inverse analysis. *International Journal of Material Forming* 12(3):355–378, doi:[10.1007/s12289-018-1421-8](https://doi.org/10.1007/s12289-018-1421-8)
- Johansson G, Ahlström J, Ekh M (2006) Parameter identification and modeling of large ratcheting strains in carbon steel. *Computers & Structures* 84(15):1002–1011, doi:[10.1016/j.compstruc.2006.02.016](https://doi.org/10.1016/j.compstruc.2006.02.016)
- Jones DR, Schonlau M, Welch WJ (1998) Efficient global optimization of expensive black-box functions. *Journal of Global Optimization* 13(4):455–492, doi:[10.1023/A:1008306431147](https://doi.org/10.1023/A:1008306431147)
- Knowles J (2006) ParEGO: a hybrid algorithm with on-line landscape approximation for expensive multiobjective optimization problems. *IEEE Transactions on Evolutionary Computation* 10(1):50–66, doi:[10.1109/TEVC.2005.851274](https://doi.org/10.1109/TEVC.2005.851274)
- Kuhn J, Spitz J, Sonnweber-Ribic P, Schneider M, Böhlke T (2021) Identifying material parameters in crystal plasticity by Bayesian optimization. *Optimization and Engineering* doi:[10.1007/s11081-021-09663-7](https://doi.org/10.1007/s11081-021-09663-7)
- Lemaitre J, Chaboche JL (1994) *Mechanics of solid materials*. Cambridge University Press
- Lophaven SN, Nielsen HB, Søndergaard J (2002) DACE-A Matlab Kriging toolbox. Tech. rep., Lyngby, Denmark
- Mahmoudi AH, Pezeshki-Najafabadi SM, Badnava H (2011) Parameter determination of Chaboche kinematic hardening model using a multi objective genetic algorithm. *Computational Materials Science* 50(3):1114–1122, doi:[10.1016/j.commatsci.2010.11.010](https://doi.org/10.1016/j.commatsci.2010.11.010)
- Marwala T, Sibisi S (2005) Finite element model updating using Bayesian framework and modal properties. *Journal of Aircraft* 42(1):275–278, doi:[10.2514/1.11841](https://doi.org/10.2514/1.11841)
- Mathern A, Steinholtz OS, Sjöberg A, Önnheim M, Ek K, Rempling R, Gustavsson E, Jirstrand M (2021) Multi-objective constrained Bayesian optimization for structural design. *Structural and Multidisciplinary Optimization* 63(2):689–701, doi:[10.1007/s00158-020-02720-2](https://doi.org/10.1007/s00158-020-02720-2)
- Ohsaki M, Miyamura T, Kohiyama M, Hori M, Noguchi H, Akiba H, Kajiwara K, Ine T (2009) High-precision finite element analysis of elastoplastic dynamic responses of super-high-rise steel frames. *Earthquake Engineering and Structural Dynamics* 38(5):635–654, doi:[10.1002/eqe.900](https://doi.org/10.1002/eqe.900)
- Ohsaki M, Miyamura T, Zhang JY (2016) A piecewise linear isotropic-kinematic hardening model with semi-implicit rules for cyclic loading and its parameter identification. *Computer Modeling in Engineering & Sciences* 111(4):303–333, doi:[10.3970/cmcs.2016.111.303](https://doi.org/10.3970/cmcs.2016.111.303)
- Paul SK, Sivaprasad S, Dhar S, Tarafder S (2011) Key issues in cyclic plastic deformation: Experimentation. *Mechanics of Materials* 43(11):705–720, doi:[10.1016/j.mechmat.2011.07.011](https://doi.org/10.1016/j.mechmat.2011.07.011)
- Rappel H, Beex LAA, Noels L, Bordas SPA (2019) Identifying elastoplastic parameters with Bayes’ theorem considering output error, input error and model uncertainty. *Probabilistic Engineering Mechanics* 55:28–41, doi:[10.1016/j.probengmech.2018.08.004](https://doi.org/10.1016/j.probengmech.2018.08.004)
- Rasmussen CE, Williams CKI (2006) *Gaussian processes for machine learning*. The MIT Press, Cambridge, Massachusetts, doi:[10.7551/mitpress/3206.001.0001](https://doi.org/10.7551/mitpress/3206.001.0001)
- Rosić BV, Kučerová A, Sýkora J, Pajonk O, Litvinenko A, Matthies HG (2013) Parameter identification in a probabilistic setting. *Engineering Structures* 50:179–196, doi:[10.1016/j.engstruct.2012.12.029](https://doi.org/10.1016/j.engstruct.2012.12.029)
- Roussel R, Hanuka A, Edelen A (2021) Multiobjective Bayesian optimization for online accelerator tuning. *Physical Review Accelerators and Beams* 24(6):062801, doi:[10.1103/PhysRevAccelBeams.24.062801](https://doi.org/10.1103/PhysRevAccelBeams.24.062801)
- Santner TJ, Williams BJ, Notz WI (2018) *The design and analysis of computer experiments*, 2nd edn. Springer, New York, NY, doi:[10.1007/978-1-4993-8847-1](https://doi.org/10.1007/978-1-4993-8847-1)
- Shahriari B, Swersky K, Wang Z, Adams RP, de Freitas N (2016) Taking the human out of the loop: A review of Bayesian optimization. *Proceedings of the IEEE* 104(1):148–175, doi:[10.1109/JPROC.2015.2494218](https://doi.org/10.1109/JPROC.2015.2494218)
- Snoek J, Larochelle H, Adams RP (2012) Practical Bayesian optimization of machine learning algorithms. In: *Proceedings of the 25th International Conference on Neural Information Processing Systems*, pp 2951–2959
- Srinivas N, Krause A, Kakade SM, Seeger M (2010) Gaussian process optimization in the bandit setting: No regret and experimental design. In: *Proceedings of the 27th International Conference on International Conference on Machine Learning*, pp 1015–1022
- Tarantola A (2005) *Inverse problem theory and methods for model parameter estimation*. SIAM, doi:[10.1137/1.9780898717921](https://doi.org/10.1137/1.9780898717921)
- Tom R (2019) Find multi-objective Pareto front using modified quicksort (MATLAB Central File Exchange). URL <https://www.mathworks.com/matlabcentral/fileexchange/73089>
- Tran A, Tran M, Wang Y (2019) Constrained mixed-integer Gaussian mixture Bayesian optimization and its applications in designing fractal and auxetic metamaterials. *Structural and Multidisciplinary Optimization* 59(6):2131–2154, doi:[10.1007/s00158-018-2182-1](https://doi.org/10.1007/s00158-018-2182-1)
- Turner BM, Zandt TV (2012) A tutorial on approximate Bayesian computation. *Journal of Mathematical Psychology* 56(2):69–85, doi:[10.1016/j.jmp.2012.02.005](https://doi.org/10.1016/j.jmp.2012.02.005)
- Vangelatos Z, Sheikh HM, Marcus PS, Grigoropoulos CP, Lopez VZ, Flamourakis G, Farsari M (2021) Strength through defects: A novel Bayesian approach for the optimization of architected materials. *Science advances* 7(41):eabk2218, doi:[10.1126/sciadv.abk2218](https://doi.org/10.1126/sciadv.abk2218)
- Villaverde AF, Fröhlich F, Weindl D, Hasenauer J, Banga JR (2018) Benchmarking optimization methods for parameter estimation in large kinetic models. *Bioinformatics* 35(5):830–838, doi:[10.1093/bioinformatics/bty736](https://doi.org/10.1093/bioinformatics/bty736)
- Voce E (1948) The relationship between stress and strain for homogeneous deformation. *Journal of the Institute of Metals* 74:537–562
- Wang M, Shi Y, Wang Y, Shi G (2013) Numerical study on seismic behaviors of steel frame end-plate connections. *Journal of Constructional Steel Research* 90:140–152, doi:[10.1016/j.jcsr.2013.07.033](https://doi.org/10.1016/j.jcsr.2013.07.033)
- Yamada S, Jiao Y (2016) A concise hysteretic model of structural steel considering the Bauschinger effect. *International Journal of Steel Structures* 16(3):671–683, doi:[10.1007/s13296-015-0134-9](https://doi.org/10.1007/s13296-015-0134-9)
- Yoshida F, Uemori T, Fujiwara K (2002) Elastic-plastic behavior of steel sheets under in-plane cyclic tension-compression at large strain. *International Journal of Plas-*

ticity 18(5):633–659, doi:[10.1016/S0749-6419\(01\)00049-3](https://doi.org/10.1016/S0749-6419(01)00049-3)
Zhang Y, Apley DW, Chen W (2020) Bayesian optimization for materials design with mixed quantitative and qualitative variables. *Scientific Reports* 10(1):4924, doi:[10.1038/s41598-020-60652-9](https://doi.org/10.1038/s41598-020-60652-9)